NAVAL POSTGRADUATE SCHOOL

MONTEREY, CALIFORNIA

THESIS

CHARACTERIZATION OF THE MEMS DIRECTIONAL SOUND SENSOR FABRICATED USING THE SOIMUMPS PROCESS

by

Antonios Dritsas

June 2008

Thesis Co-Advisors:	Gamani Karunasiri
	Robert Koyak

Approved for public release; distribution is unlimited

THIS PAGE INTENTIONALLY LEFT BLANK

REPORT DOCUMENTATION PAGE		*Form Approved OMB No. 0704-0188*
Public reporting burden for this collection of information is estimated to average 1 hour per response, including the time for reviewing instruction, searching existing data sources, gathering and maintaining the data needed, and completing and reviewing the collection of information. Send comments regarding this burden estimate or any other aspect of this collection of information, including suggestions for reducing this burden, to Washington headquarters Services, Directorate for Information Operations and Reports, 1215 Jefferson Davis Highway, Suite 1204, Arlington, VA 22202-4302, and to the Office of Management and Budget, Paperwork Reduction Project (0704-0188) Washington DC 20503.

1. AGENCY USE ONLY *(Leave blank)*

2. REPORT DATE
June 2008

3. REPORT TYPE AND DATES COVERED
Master's Thesis

4. TITLE AND SUBTITLE Characterization of the MEMS Directional Sound Sensor Fabricated Using the SOIMUMPS Process

5. FUNDING NUMBERS

6. AUTHOR(S) Antonios Dritsas

7. PERFORMING ORGANIZATION NAME(S) AND ADDRESS(ES)
Naval Postgraduate School
Monterey, CA 93943-5000

8. PERFORMING ORGANIZATION REPORT NUMBER

9. SPONSORING /MONITORING AGENCY NAME(S) AND ADDRESS(ES)
N/A

10. SPONSORING/MONITORING AGENCY REPORT NUMBER

11. SUPPLEMENTARY NOTES The views expressed in this thesis are those of the author and do not reflect the official policy or position of the Department of Defense or the U.S. Government.

12a. DISTRIBUTION / AVAILABILITY STATEMENT
Approved for public release; distribution unlimited

12b. DISTRIBUTION CODE

13. ABSTRACT (maximum 200 words)

A micro-electro-mechanical system (MEMS) based directional sound sensor performance is characterized. The operation of directional sound sensor is based on the hearing organ of *Ormia ochracea* fly, which uses coupled bars hinged at the center to achieve the directional sound sensing.

The MEMS sensor design considered in this thesis is fabricated using a process by which the sensor has two resonant vibrational modes: rocking and bending. The sensor is simulated using finite element analysis and tested by actuating the sensor using a sound stimulus. An analysis is undertaken to describe, in mathematical terms, the relationship between the sensor's amplitude of vibration and various parameters such as the angle of incidence, frequency and the intensity of sound.

The experimentally-observed vibrational frequencies are found to be in good agreement with the simulated data, which supports the use of the simulation in future sensor development. The observed amplitudes of vibration are significantly greater than those of sensors fabricated with the process used in previous studies. The relationship between the amplitude of vibration and the incident angle are found to agree with the theoretical predictions. The results indicate that it is possible to fabricate miniature sound sensors that mimic the fly's hearing system.

14. SUBJECT TERMS SOIMUMPs, MEMS, Ormia Ochracea, Biomimetic, Directional Microphone, Sensors, Microphone, Fly Hearing, Undersea Warfare

15. NUMBER OF PAGES
113

16. PRICE CODE

17. SECURITY CLASSIFICATION OF REPORT Unclassified	**18. SECURITY CLASSIFICATION OF THIS PAGE** Unclassified	**19. SECURITY CLASSIFICATION OF ABSTRACT** Unclassified	**20. LIMITATION OF ABSTRACT** UU

NSN 7540-01-280-5500

Standard Form 298 (Rev. 2-89)
Prescribed by ANSI Std. 239-18

THIS PAGE INTENTIONALLY LEFT BLANK

CHARACTERIZATION OF THE MEMS DIRECTIONAL SOUND SENSOR FABRICATED USING THE SOIMUMPS PROCESS

Antonios Dritsas
Lieutenant, Hellenic Navy
B.S. in Applied Sciences, Hellenic Naval Academy, 1998

Submitted in partial fulfillment of the
requirements for the degree of

MASTER OF SCIENCE IN APPLIED PHYSICS
and
MASTER OF SCIENCE IN OPERATIONS RESEARCH

from the

NAVAL POSTGRADUATE SCHOOL
June 2008

Author: Antonios Dritsas

Approved by: Gamani Karunasiri
                 Thesis Co-Advisor

                 Robert Koyak
                 Thesis Co-Advisor

                 James H. Luscombe
                 Chairman, Department of Physics

                 James N. Eagle
                 Chairman, Department of Operations Research

THIS PAGE INTENTIONALLY LEFT BLANK

ABSTRACT

A micro-electro-mechanical system (MEMS) based directional sound sensor performance is characterized. The operation of directional sound sensor is based on the hearing organ of *Ormia ochracea* fly, which uses coupled bars hinged at the center to achieve the directional sound sensing.

The MEMS sensor design considered in this thesis is fabricated using a process by which the sensor has two resonant vibrational modes: rocking and bending. The sensor is simulated using finite element analysis and tested by actuating the sensor using a sound stimulus. An analysis is undertaken to describe, in mathematical terms, the relationship between the sensor's amplitude of vibration and various parameters such as the angle of incidence, frequency and the intensity of sound.

The experimentally-observed vibrational frequencies are found to be in good agreement with the simulated data, which supports the use of the simulation in future sensor development. The observed amplitudes of vibration are significantly greater than those of sensors fabricated with the process used in previous studies. The relationship between the amplitude of vibration and the incident angle are found to agree with the theoretical predictions. The results indicate that it is possible to fabricate miniature sound sensors that mimic the fly's hearing system.

THIS PAGE INTENTIONALLY LEFT BLANK

TABLE OF CONTENTS

LIST OF FIGURES

LIST OF TABLES

THIS PAGE INTENTIONALLY LEFT BLANK

LIST OF ABBREVIATIONS AND ACRONYMS

ASW   Anti-Submarine Warfare

AUV   Autonomous Underwater Vehicle

DRIE   Deep Reactive Ion Etching

FAS   Federation of American Scientists

FEM   Finite Element Modeling

ICP   Inductively Coupled Plasma

MEMS   Micro-Electro-Mechanical Systems

PolyMUMPs Polysilicon Multi-User MEMS Process

PSG   Phosphosilicate Glass

PTM   Prosternal Tympanal Membranes

RIE   Reactive Ion Etched

SOI   Silicon-On-Insulator

SOIMUMPs Silicon-On-Insulator Multi-User MEMS Process

TASS   Towed Array Sonar Systems

UAV   Unmanned Aerial Vehicles

VHF   Very High Frequency

THIS PAGE INTENTIONALLY LEFT BLANK

ACKNOWLEDGMENTS

I would like to thank Professor Gamani Karunasiri for his physics guidance, support, and patience during the course of this research effort.

I would like to thank Professor Robert Koyak for his support, guidance and insightful contribution throughout this research. It has been a real privilege working with you.

I would like also to thank Breen Dix for keeping an eye on any grammatical or syntactical errors and Nancy Sharrock for assisting me in formatting the write-up of this thesis.

I would like to express my gratitude and love to my beloved wife Anthi for giving me all the support I could have ever asked for.

THIS PAGE INTENTIONALLY LEFT BLANK

EXECUTIVE SUMMARY

There is a wide range of potential military applications to situations where ambiguity in bearing occurs with respect to sound. For example, autonomous unmanned aerial vehicles (UAVs) could employ a sensor to determine the bearing of an explosion and conduct battle damage assessment (BDA) on it. With existing sensors this is difficult to do because the explosion is too short in duration to use the Doppler Effect to determine the bearing. Also, an autonomous underwater vehicle (AUV) acting as a quiet platform to tow a short omni-directional hydrophone array must contend with bearing ambiguity. If a directional microphone that eliminated the bearing ambiguity were developed and added to the towed array, the integrated system would constitute a valuable acoustic measurement tool.

In this thesis, characterization of a directional sound sensor using micro-electro-mechanical systems (MEMS) technology based on the hearing system of a small fly (*Ormia ochracea*) is described. The fly uses coupled bars hinged at the center to achieve the directional sound sensing by discriminating the vibration amplitude of each bar. The sensors used in this thesis are fabricated using Silicon on Insulator Multi-User MEMS Processes (SOIMUMPs) technology available through MEMSCAP [MEMSCAP, 2004]. The wings of the sensor are made primarily of solid silicon plate in order to maximize the vibration amplitude when the substrate underneath them is removed. A set of sensors with perforated wings is also included in the design to gauge the sound coupling efficiency.

The sound sensor is found to have two resonant vibrational modes (rocking and bending). The sensor is simulated using finite element analysis and tested by actuating the sensor using a sound stimulus. The purpose of the simulation is to obtain a valid representation of the sensor under study that could be used in future sensor development. An analysis to describe the relationship between the sensor's amplitude of vibration and various parameters as the angle of incidence and the intensity of sound was conducted.

Experiments as well as simulation using finite element software are conducted to assess the performance when two prototypes located on a single chip are tested under varying conditions.

The experimentally observed vibrational frequencies are found to be in good agreement with those of the simulated sensor. The amplitudes of vibration are found to be of the same order of magnitude compared with the simulated sensor and significantly larger than values reported in previous studies that employed sensors fabricated using the PolyMUMPs process. The amplitude of vibration is found to increase as the incident angle is increased and follows in good agreement the theoretical predictions.

Some differences between the two prototypes are found especially as the frequency diverges from the resonant frequency (2980 Hz) of the sensor. This analysis points out some disadvantages of the current set up of the physical experiment. Some changes regarding the position of the sensor and the absorbing material that is used are made to attain more reliable experimental units. The model developed in this thesis uses as a response variable the natural logarithm of the vibration amplitude of the sensor. In order to find a goodness-of-fit measure that applies to the response variable directly, estimates on the logarithmic scale are converted back to the original units. Because a logarithmic transformation is used, it is appropriate to consider a measure that expresses the explanatory power of the model in relative terms. The statistical model developed in this thesis achieves an average relative error (ARE) of 3.80 percent, which implies that the model is capable of predicting the vibrational amplitude of the sensor with an error that averages 3.80 percent of the actual value. This suggests that the model provides an adequate representation of the behavior of the sensor.

At the last stage of the thesis research, a second chip of design identical to the chip under study is analyzed. A regression analysis is conducted in order to characterize similarities and differences between the two identical sensors located on the chip. This analysis reveals almost identical performance from the two sensors in a band of frequencies near the resonant frequency. It is also shown that the vibrational amplitudes

of the two wings of each sensor differ significantly, which is a key factor in the fabrication of a sensor with improved bearing determination. The ARE for this last model is 6.25 percent.

The thesis research suggests that it is feasible to fabricate a MEMS-based sensor that mimics the fly's hearing organ. However, the successful development of an integrated system of sound sensors that resolves the bearing ambiguity problem requires additional research in sensor design. In particular, a broader range of response around the resonant frequencies must be achieved to enhance the coupling of the two vibrational modes. This enhanced coupling would increase the difference of the amplitudes associated with the two wings of the sensor, leading to improved bearing resolution.

The sensor fabricated using the SOIMUMPs process is found to provide greater amplitudes compared to the PolyMUMPs-based sensors, and is therefore better suited for resolving the problem of bearing ambiguity. However, sensors designed with either process that rely on damping due to air to produce large amplitude differences between the two wings may not be able to compensate for sharp responses near the resonant frequencies. Additional mechanisms such as squeezed-film damping are needed to increase overlapping near the two modes of vibration. However, the perforated holes on the wings needed to produce squeezed-film damping also severely reduces the amplitude of vibrations due to the leaking of sound pressure through the holes, which degrades performance of the sensor. The answer might be to put holes in a relatively small part of the wings and leave the substrate intact in those areas. Simulations reveal that such a configuration provides a sensor with a broader frequency response curve. Further research is needed to confirm the simulated performance of the sensor.

THIS PAGE INTENTIONALLY LEFT BLANK

I.   INTRODUCTION

A.   INTRODUCTION

This thesis examines the performance of a directional sound sensor that was developed to overcome the shortcomings of existing sensors. The development of an effective directional sound sensor has important military applications, in particular to anti-submarine warfare (ASW). The sensor considered in this thesis is modeled on the hearing system of a small fly (*Ormia ochracea*) using a micro-electromechanical systems (MEMS) technology. Experiments based on prototypes of this sensor are conducted to gain insight into its properties. The experimental data are analyzed to assess the effectiveness of the sensor and to suggest directions for its further development.
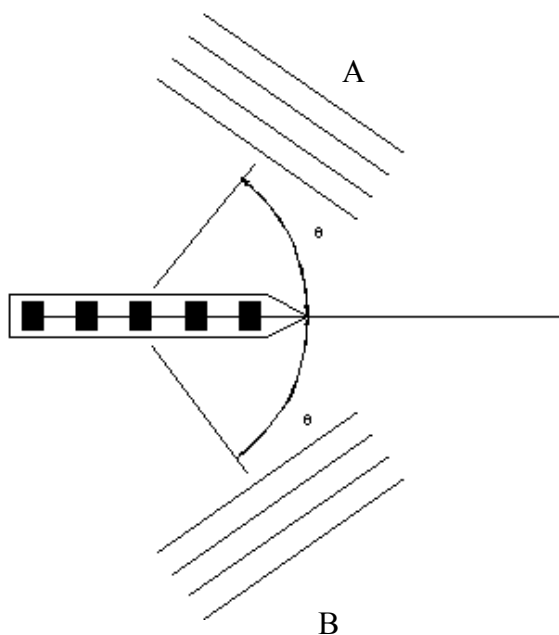
Figure 1.   Bearing Ambiguity with Towed Array Systems (After: Federation of American Scientists (FAS), 2008)

Locations A and B are potential sound sources that project a stimulus toward the Towed Array System. If the sound is incident from point A the system will not be able to determine if the sound is actually coming from point A or its reflection, which is B (same angle θ along x-axis).

1

In ASW, sound sensors such as active or passive sonar, towed array sonar systems (TASS), and self-contained sonar systems (sonobuoys) are used to locate targets. Currently, TASS used for directional sensing employs a linear array of omni-directional hydrophones as shown in Figure 1. Because the array is linear, it lacks the ability to determine vertical directionality. This causes two problems: (a) bottom-bounce propagation, in which case the direction of the source is not known without further analysis, and (b) ambiguity in relative bearing: the omni-directional hydrophones cannot distinguish signals on the left from those on the right, or from signals on the top from those on the bottom.

The problem of bearing ambiguity can be resolved by maneuvering the ship and using an application of the Doppler effect of sound. The maneuvering of the ship towards or away from the target causes a frequency shift in the received signal, which is an indication of the position of the target. More explicitly, an increasing frequency indicates that the ship is approaching the target, whereas a decreasing frequency indicates that the ship is diverging from the target. Moreover, as the ship changes its position, there will again be two ambiguous bearings as shown in Figure 1, but only one of which will match the previous case. Comparing each time the bearings of the current position with those of the previous one, the right location of the target is indicated by the two crossing bearings. These two techniques can work well as long as the target has not moved significantly before and after the maneuver of the ship, but they can lead to inaccurate conclusions if the target is moving at a relatively high speed.

Sonobuoys that are used in directional sound sensing are small, self-contained sonar systems that are dropped into the water by an aircraft, at which point they deploy themselves [FAS, 2008]. The information from the sonobuoys can be transmitted either to aircraft or to ships by very high frequency (VHF) radio link. Mostly because of their limited size, sonobuoys have poor directional sensing, so it would be desirable to couple them with a small directional sound sensor having low power consumption to improve their performance in direction finding.

Although development of an improved sensor as described above is of great interest in the ASW environment, there is a wide range of potential military applications

to situations where ambiguity in bearing occurs with respect to sound. For example, autonomous unmanned aerial vehicles (UAVs) could employ the sensor to determine the bearing of an explosion and conduct battle damage assessment (BDA) on it. Additionally, an autonomous underwater vehicle (AUV) could act as a quiet platform to tow a short hydrophone array. If a directional microphone were developed and added to the towed arrays of the AUV, the integrated system would result in a valuable acoustic measurement tool.

B.   BACKGROUND

Animals use their hearing to pinpoint an auditory stimulus when both of the ears are excited by a sound wave. Two factors that have an important role in the localization of a sound are the differences in arrival times and in the intensity of the sound, between the nearest and the furthest ear, with respect to the sound source. In the case of large animals, where the distance between the two ears is large enough compared with the sound wavelength, the differences in intensity and the arrival time between the ears are substantially large and easily detected, resulting in the localization of the sound source. On the other hand, a small animal cannot locate a sound sensor this way, since the distance between its ears is relatively small compared to the wavelength of the sound wave, and leads to a very small interaural difference in intensity and arrival time of the sound [Miles, Robert and Hoy, 1995]. As a result, many small animals, including *Ormia orchracea*, have developed mechanisms for effectively increasing these differences before the sound stimulus reaches the auditory cells [Michelsen, 1992]. The biological motivation for sound localization in *Ormia ochracea* is that, for reproductive purposes, the female flymust deposit her parasitic larvae on a live cricket [Cade, 1975]. Apparently, because of the black color of the crickets, the fly locates her host at night, relying only on acoustical cues from the cricket's mating call.

1.   The Auditory System of *Ormia Ochracea*

The acoustico-sensory organs in *Ormia ochracea* are extremely small. The fly's left and right ear are contained within a common air-filled chamber separated 500 μm

from each other. Another difference in the fly's auditory system relative to other animals is the placement of the ears, not on the head but on the front face of the thorax directly behind the head [Miles, Robert and Hoy, 1995]. A comprehensive description of the ear anatomy of *Ormia ochracea* is given in Robert, Read and Hoy, (1994).
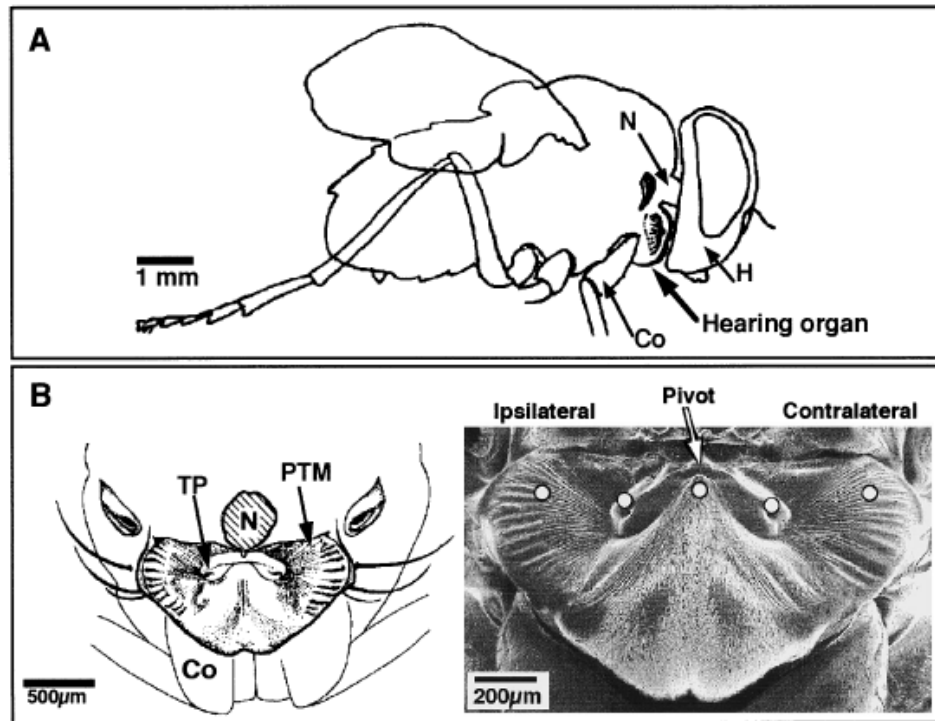
Figure 2.   Location and External Anatomy of the Ears of *Ormia Ochracea* (From: Miles, Robert and Hoy, 1995)

> In Figure B, frontal views of the ears with the head removed. Left panel is a line drawing; right panel is a scanning electron micrograph. The posternal tympanal membranes (PTM) show radial corrugations. These corrugations converge upon the tympanal pit (TP) to which, internally, the sensory organ is attached. Ipsilateral and contralateral PTM are shown in respect to a hypothetical sound source from the left.

The anatomy of the ears and their size is such that the fly cannot reliably attain directional information based on the difference in arrival times and intensity of sound wave at each ear. Instead, the fly is able to increase the time delay for the effect of sound traveling from the ear nearest to the sound source (ipsilateral) to the ear farthest from the sound source (contralateral) using a mechanical coupling between the ear drums (tympana) [Miles, Robert and Hoy, 1995].

4

The mechanical coupling consists of a flexible mechanical bar that connects the two sensory ears and pivots around a hinge. Figure 2 shows (A) the line drawing of the fly illustrating the exact location of the acoustic organ and (B) the frontal views of the ears both as a line drawing (on the left panel) and as a scanning electron micrograph (on the right panel). In Figure 2B, the central dot represents the pivotal point for the mechanical bars, which are shown with the second layer of dots (one on each side). The two external dots represent a pair of prosternal tympanal membranes (PTM), which operate as an eardrum, driving the solid bars around the pivotal point via the incident sound wave [Miles, Robert and Hoy, 1995].

2. Mechanical Model

The mechanical model in Figure 3 represents a simplified version of the fly's ear system.
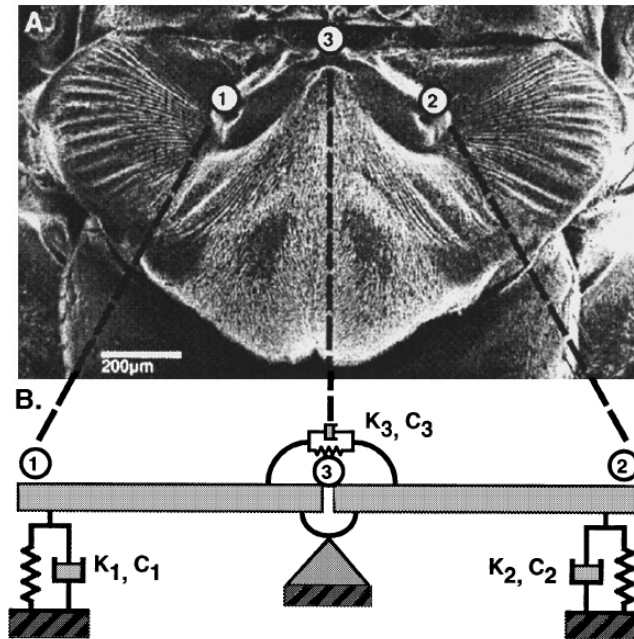
Figure 3.   Mechanical Model Representing Fly's Auditory System (From: Miles, Robert and Hoy, 1995)

K_i, C_i are the spring and damping constants of the equivalent mechanical model of the fly's ear system respectively.

5

The primary elements of the mechanical model are the two rigid bars (points 1 and 2 in Figure 3) connected at the pivot (point 3 in Figure 3), which ideally represents the intertympanal bridge.

The springs and the dampers located at the end points 1 and 2 represent the dynamical performance of the tympanal membranes and the surrounding structures. According to the model in Figure 3, when the sound arrives at the left rigid bar (ipsilateral eardrum), its movement produces forces on the right bar (contralateral eardrum) via the pivot point (intertympanal bridge) which oppose the initial forces on the left bar caused by the external pressure received there.

The model in Figure 3 takes into account the basic elements of the fly's auditory system which are believed to hold the most kinetic and potential energy from the vibrations caused by a sound stimulus [Robert, Read and Hoy, 1994; Miles, Robert and Hoy, 1995]. The mechanical equivalent of the fly's auditory system is a two-degree of freedom spring-mass-damper system as described in Rao (2003). A detailed description of the fly's mechanical model can be found in Shivok (2007). In the following section, key features of the physics behind the model are described.

3.   Physical Description of the Mechanical Model

Figure 4 shows the fly's equivalent mechanical model displaced by the incident sound wave at time t. Because the left and the right ears are physiologically identical, the spring and damping coefficients of them (K_s, C_s) are taken to be the same. Additionally, K_3 and C_3 of Figure 3 can be renamed K_t, C_t, which represent the parameters of the intertympanal bridge.

6
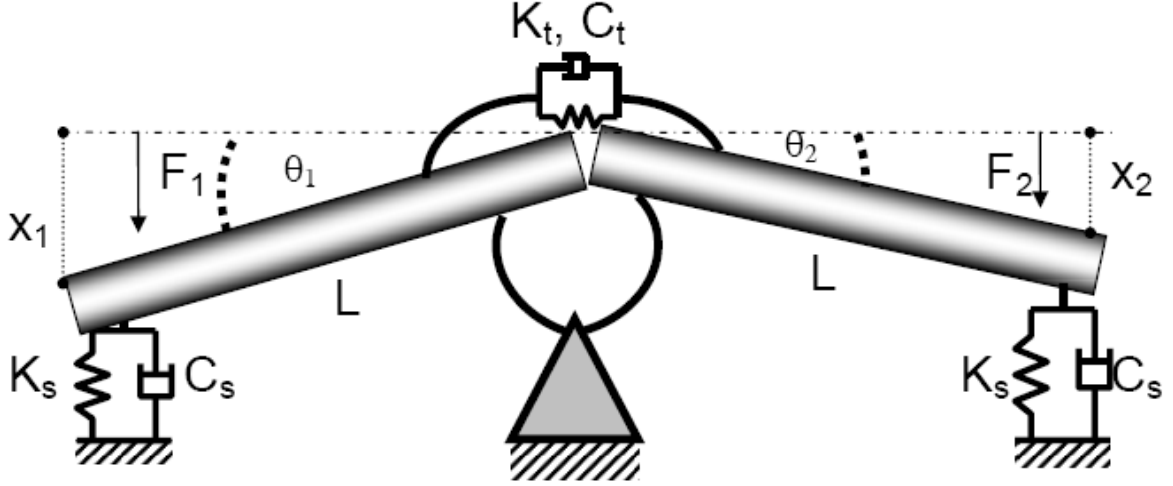
Figure 4. Mechanical model representing fly's auditory system (After: Miles, Robert and Hoy, 1995)

Taking into consideration the forces on the rods due to the compressions and expansions of the springs and dampers, the equation of motion for the two rods can be written as:

$$m_1\ddot{x}_1 + (C_w + C_t)\frac{dx_1}{dt} + C_t\frac{dx_2}{dt} + (K_w + K_t)x_1 + K_t x_2 = F_1 \tag{1.1}$$

$$m_2\ddot{x}_2 + (C_w + C_t)\frac{dx_2}{dt} + C_t\frac{dx_1}{dt} + (K_w + K_t)x_2 + K_t x_1 = F_2. \tag{1.2}$$

Solving this system of equations and considering that the masses of the bars are equal ($m_1 = m_2 = m$), gives the first two frequencies, or Eigen modes, as:

$$\omega_{Rocking} = \sqrt{\frac{K_s}{m}}, \quad \omega_{Bending} = \sqrt{\frac{K_s + 2K_t}{m}}. \tag{1.3}$$

A detailed proof of Equation 1.3 is given in Miles, Robert and Hoy (1995). Interpreting the Equation 1.3, the rocking motion depends only on the two springs at the edges, while the bending motion depends also on the one at the center.
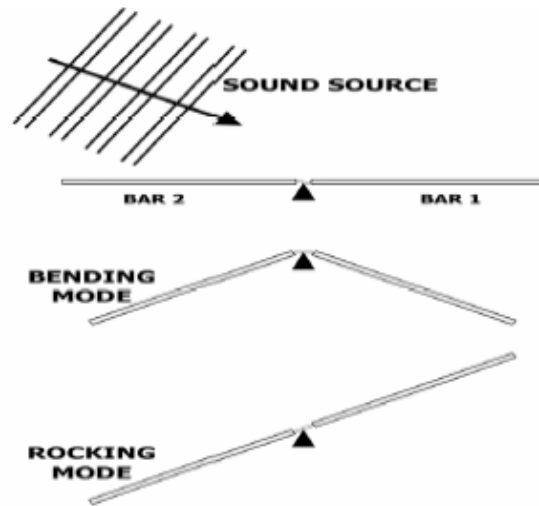
Figure 5.   Ear Vibration Eigen Frequency Modes (From: Shivok, 2007)

A representation of a visual of the bars at an instance in time for each of
the two natural modes of vibration of *Ormia ochracea*'s auditory system.

The rocking motion of the coupled bars of the fly's auditory system resembles a
seesaw as it rocks back and forth while the bending mode is similar to a bird bending its
wings for flight. The following chapter outlines the design and fabrication of a sound
sensor based on Micro-electro-mechanical systems (MEMS) technology; that mimics the
fly's auditory system.

II.   MEMS DESIGN

A.   INTRODUCTION

MEMS based directional sound sensors are fabricated to replicate the sensory properties of the ear of the *Ormia ochracea* fly. This chapter outlines the process of fabricating MEMS sensors, and the experimental design for the collection of data used to evaluate the performance of these sensors. MEMS sensors can be fabricated using a number of different materials and manufacturing techniques, the choice of which will depend on the device being created and the environment in which it is to operate. Taking into account the very small size of the fly's hearing organ, MEMS technology is highly suitable for development of a biomimetic sound sensor. The sensors described in this thesis were fabricated using Silicon on Insulator Multi-User MEMS Processes (SOIMUMPs) technology available through MEMSCAP [MEMSCAP, 2004].

B.   INTRODUCTION TO THE SOIMUMPS PROCESS

Previous studies have demonstrated that it is possible to design and fabricate a biomimetic MEMS sensor that displays the expected rocking and bending modes of vibration similar to those of the ear of *Ormia ochracea* [Miles, Robert, Hoy, 1995]. The design consists of a rectangular plate with two legs hinged in the middle to a substrate as shown in Figure 6. The plate is released at the end of the MEMS fabrication process, allowing it to oscillate when excited by a sound source. Detailed information on the design and testing of a sensor built using PolyMUMPs technology can be found in Shivok (2007). A drawback of the PolyMUMPs sensor is its relatively small amplitudes of vibration under sound excitation, due primarily to the front side holes used for reducing squeezed film damping. Simulations have shown that a solid plate structure would provide better sound coupling, although it requires the etching of holes through the substrate or entirely removing it to reduce the damping. The latter is conveniently achieved using a SOIMUMPs fabrication process available at the same foundry. In the following subsections, the basic features of the SOIMUMPs process are described.

9
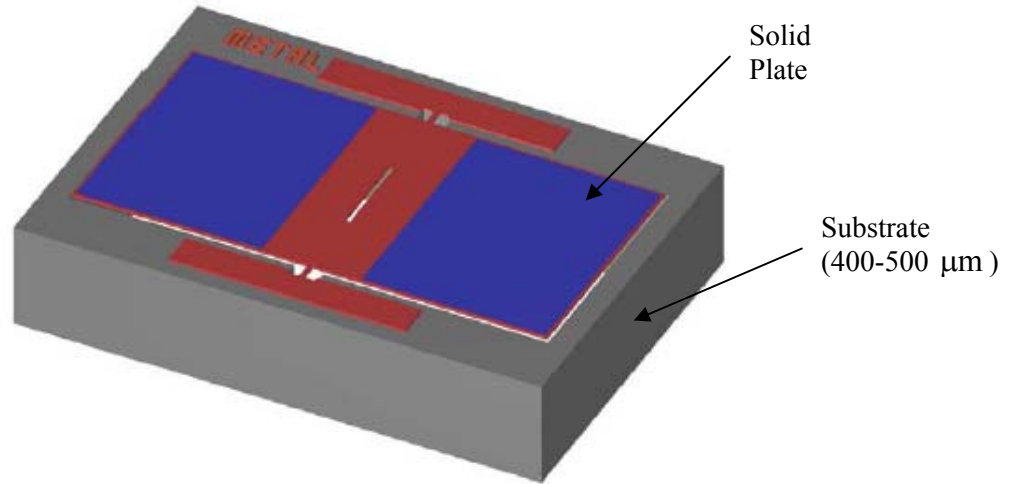
Figure 6.   Biomimetic Sound Sensor Layout of *Ormia ochracea*

The substrate of the device underneath the solid silicon plate has been removed to allow for an increase of the vibration amplitude of the sensor.

1.   SOIMUMPS Process Definition

The SOIMUMPS process starts with a silicon-on-insulator (SOI) substrate [Miller et al., 2004]. The substrate acts as the base on which the whole structure is built. It is approximately 400 micrometers in depth. At the top of the substrate is a 1 micrometer oxide layer and above that a 10 or 25 micrometers silicon device layer, as illustrated in Figure 7. The silicon layer can be used for the fabrication of the wings of the sound sensor. A bottom oxide layer that is slightly thinner than the oxide layer below the device layer is also present on the bottom side of the substrate. This is used to protect the unexposed areas of the substrate during the trench etching through the substrate.

The SOIMUMPs fabrication process begins with the top surface of the silicon layer, which is doped by depositing a phosphosilicate glass (PSG) layer and annealing at 1050˚C for 1 hour in argon. This PSG layer is then removed through the use of wet chemical etching.

10

Metal 0.5 – 1 micrometers
Silicon Layer 10 or 25 micrometers
Oxide Layer 1 micrometer
Substrate Layer 400 micrometers
Bottom Oxide Layer < 1 micrometer

Figure 7.   SOIMUMPs Layering and Thickness

The pad metal is then deposited which must be covered during the subsequent deep reactive ion etching (DRIE) of the silicon layer. The pad metal is not deposited if the device does not require electrical contacts. Next, the silicon layer is lithographically patterned with the second mask level (SOI) and etched using the DRIE process to define the wings of the sensor. This etching is performed using inductively coupled plasma (ICP) technology, and a special SOI formulation is used to virtually eliminate any undercutting of the silicon layer when the etch reaches the oxide [Miller et al., 2004].

Next, a front side protection material is applied to the top surface of the silicon layer to protect it during the trench etching of the substrate. The wafers are then reversed, and the substrate layer is lithographically patterned from the bottom side using the third mask level, trench. A reactive ion etched (RIE) process is used to remove the bottom oxide layer in the regions defined by the trench mask followed by DRIE to etch the trench pattern through the substrate. The front side protection material is then stripped in a dry etch process. This releases any mechanical structures in the silicon layer that are located over through holes defined in the substrate layer [Miller et al., 2004]. Additional metal deposition is available via a shadow mask process for making electric contact to the substrate as well as the device layers. A more detailed description of how the layers in the SOIMUMPs process are created can be found in the SOIMUMPs design handbook [Miller et al., 2004].

C.   MEMS SOUND SENSOR DESIGN

As described in Chapter I, the tympanal membranes of the fly's auditory system convert the sound wave, and more precisely the sound pressure, into displacement of the two bars. An equivalent mechanical system can be designed using MEMS to convert sound pressure into a displacement as illustrated in Figure 6.

The basic design of the structure to be fabricated using SOIMUMPs is depicted in Figure 8.
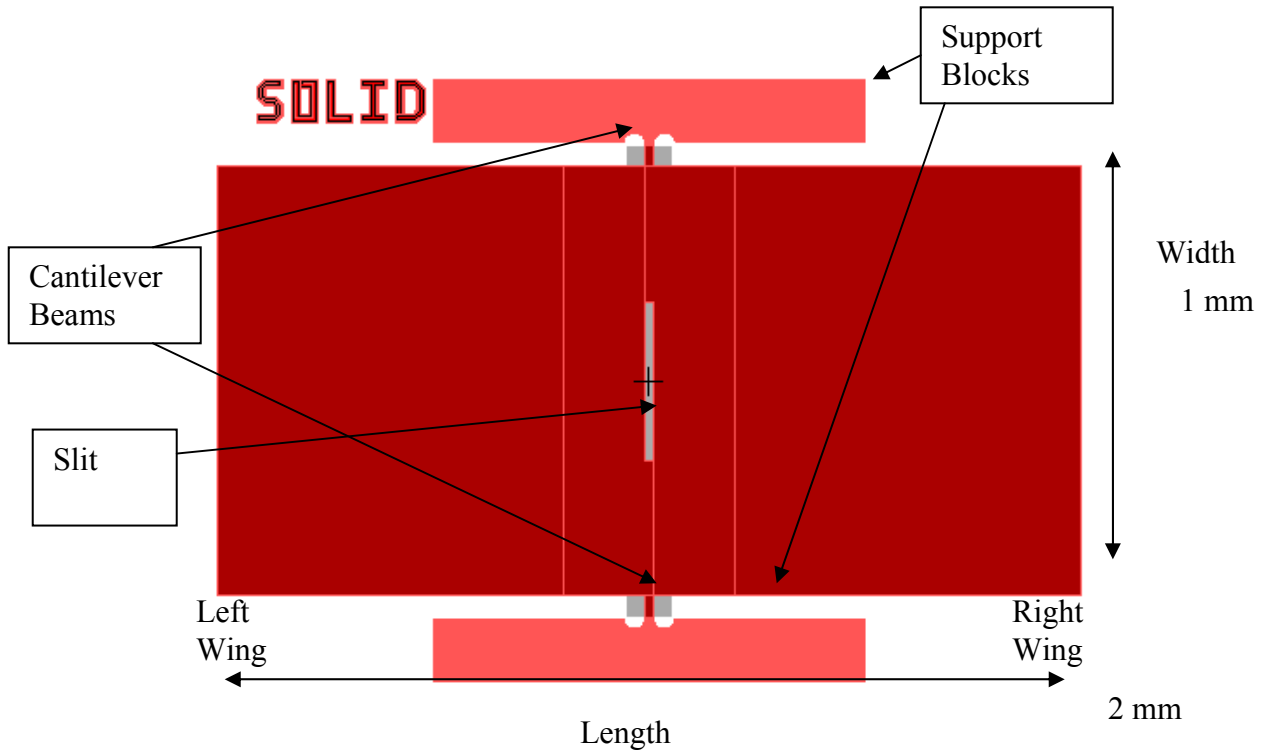
Figure 8.   SOIMUMPs Design of Directional Sensor with solid wings

Two wings (1 mm2 each) act like the bars and the tympanal membranes in the fly's ears. The thickness of the wings is determined by the device layer thickness, which is 10 microns. The two wings are attached to the substrate using two hinges with lengths of 75 microns and widths of 20 micron. The wings do not have holes in them as in the previous designs (using PolyMUMPs) because the control of the damping (K_s) in this case is achieved by etching the substrate under the silicon wings. The beams connecting

the support block and the wings, acting as torsional springs with stiffness C_S, determine the rocking resonant frequency. The bending resonant frequency is primarily controlled by the width and thickness of the wings, which can be controlled by etching a slit in the middle to reduce the "effective width". In the present design a slit with 370 microns length and 20 microns width is employed. The values of spring constants are determined primarily by the material properties of the silicon in addition to the component dimensions. Figure 9 gives a cross-section view of the device showing the trench underneath of the wings due to removal of the substrate. The damping of the system is due primarily to the air drag as the wings oscillate with the sound frequency.
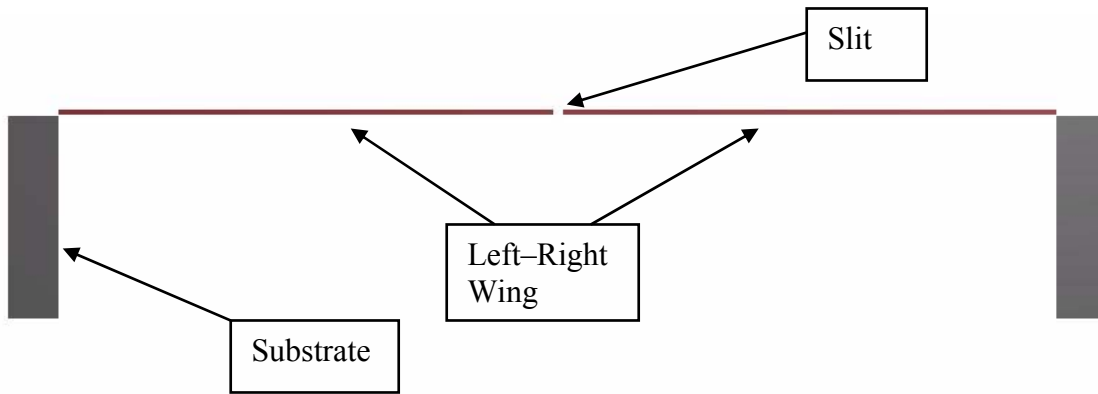
Figure 9.   Cross Section of Directional Sensor

Representation of a horizontal cross section through the center of the directional sensor of the above Figure 3. This view shows the air gap underneath the two wings caused by the trench of the substrate.

In addition to the solid plate wings, a set of sensors was also designed with different size holes on the wings. The holes used in these structures are much smaller than those employed in the earlier PolyMUMPs design. In these structures, there is no trench under the wings and the holes provide a path for the air under the wings to escape. This allows us to control the damping for achieving the desired response by properly mixing the rocking and bending motions [Miles, 1995]. When the wings move, the air

underneath the wings squeezes through the holes, which generates squeezed film damping [Rao, 2003]. However, such an arrangement still can reduce the coupling of sound field with the wings as observed in the previous design.

Because control of damping is very important for the mixing of the rocking and bending motions, multiple device designs with different hole dimensions were created as shown in Figure 11. Each of these different designs was based on the device shown in Figure 8, with slight modifications in an attempt to find the optimal configuration.
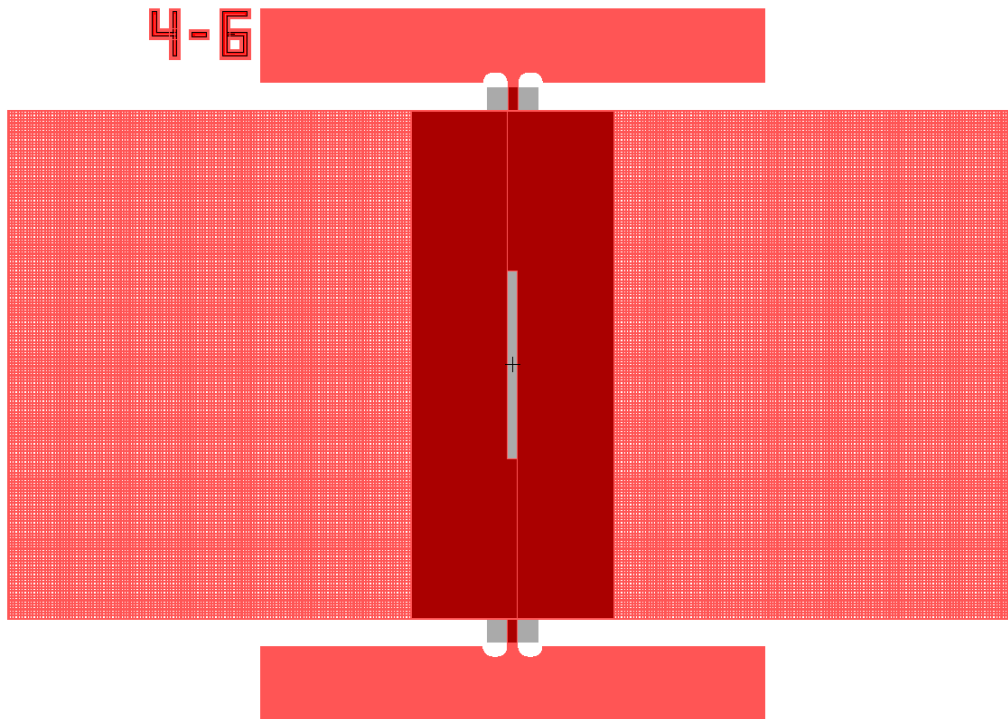
Figure 10.   Alternative Design of Directional Sensor with Perforated Wings

D.   CHIP LAYOUT

Achieving the proper value of damping in a MEMS sensor is critical to the accurate determination of the bearing of the sound source. Because this value was not known *a priori*, it was necessary to fabricate multiple designs to empirically determine

14

the combination of holes size, number of holes, etc. which provides the best performance. For this reason, 15 different devices, each with a different design, were placed on a single chip for testing purposes. Figure 11 shows the layout of the devices on a chip.
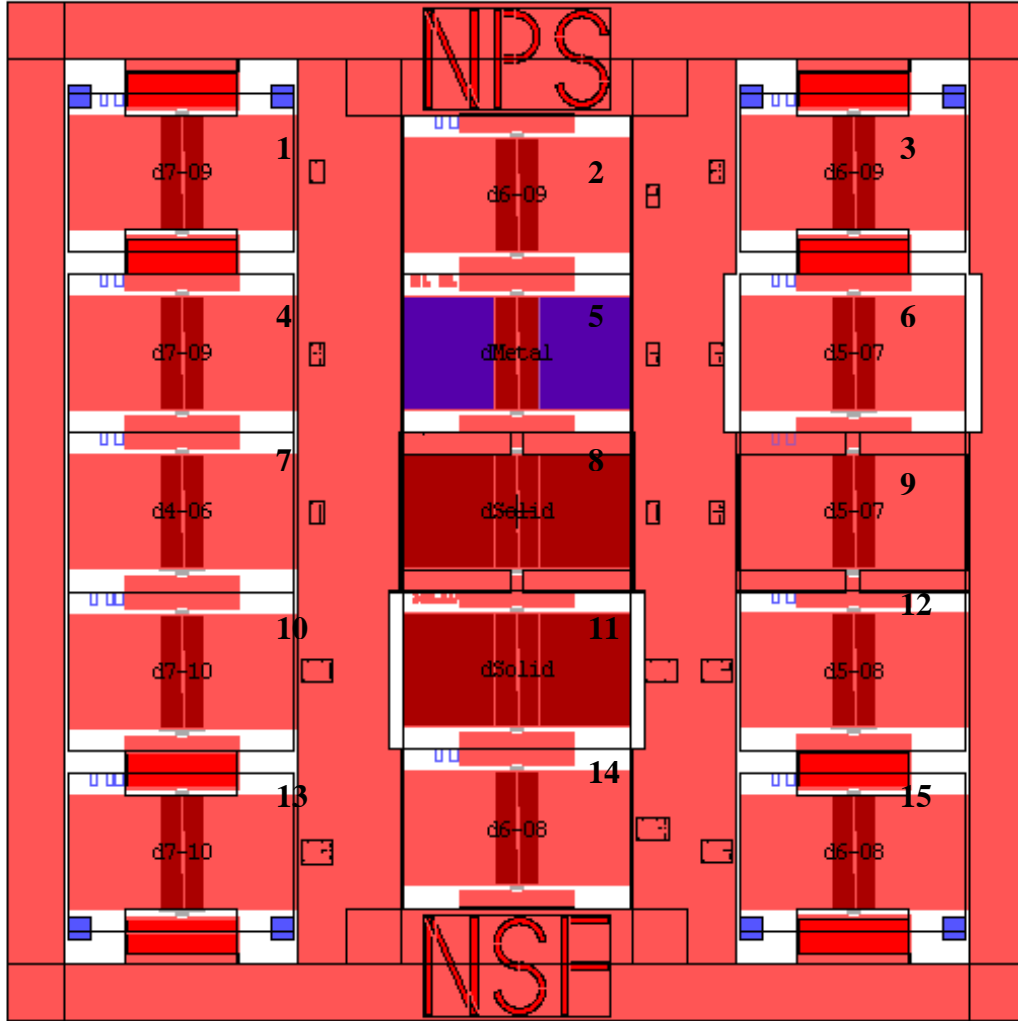
Figure 11.   Chip Layout with Fifteen Sensors

> The first number in its sensor represents the side's size for squared shape holes while the second number represents the distance between the centers of two adjacent holes. All the numbers are expressed in microns.

Device number 8 is the primary design, shown in Figure 8.   The parameters defining the different devices are listed in Table 1.

Sensor	Holes	
	Size (μm)	Distance (μm)
1	7	9
2	6	9
3	6	9
4	7	9
5	Metal	Metal
6	5	7
7	4	6
8	Solid	Solid
9	5	7
10	7	10
11	Solid	Solid
12	5	8
13	7	10
14	6	8
15	6	8

Table 1.   Design Parameters used for the Chip in Figure 11

For all the sensors the cantilever beams are 75 microns in length and 20 microns wide. The dimension of each sensor is the same with the primary design that is discussed in Figure 8 with length and width 2 and 1 mm, respectively.

In the following chapter, the simulation of device number 8, which is considered as the primary design, is discussed, using the respective design parameters of Table 1 above.

III.   COMSOL SIMULATION

A.   INTRODUCTION

Once the characteristics of the biomimetic sensor were discussed, it is essential to test the sensor, conducting a series of simulations. The purpose of the simulation mainly is to obtain a valid representation of the sensor under study that could be used in future sensor development. For this reason, a unifying multiphysics simulation environment is used, called COMSOL. A more detailed description of COMSOL software package and the process that is followed during the simulations is presented later in this chapter. A large number of simulations are conducted in order to characterize the response of the sensor and also to verify the existence of the sensor's resonance frequencies (rocking and bending). Another set of simulations tests the dependence of the displacement of the sensor's wings with the incident angle of sound. A critical part of the simulation problem is the estimation of an equation expressing the sensor's air damping coefficient [Zhang and Turner, 2004] and its relationship with the air pressure that is applied [Newell, 1968].

B.   AIR DAMPING CONSIDERATIONS

In physics and engineering, damping may be mathematically modeled as a force (F) synchronous with the velocity (v) of an object but opposite in direction to it. Thus, in the general case of a mechanical damper, the force is proportional to the velocity and is given by equation $F = -cv$, where c is called damping coefficient. Respectively for the sensor that is described in Chapter II, air damping is the force that is applied to the surface of the sensor's wings by the surrounding air. This force will be proportional to the sensor's velocity of vibration but opposite in direction.

Air damping is probably the most significant factor in determining the dimensions and specifically what degree of miniaturization is the lowest allowable for the designed device [Newell, 1968]. It is well known in MEMS that air damping increases rapidly as the device's volume-to-surface ratio decreases. In order to analyze how the damping of a

17

device varies with ambient air pressure, it is essential to divide the pressure range from vacuum to atmospheric pressure into three regions. Newell [1968] identifies the effects of damping that are characteristic of the three regions.

In the first region, the pressure is so low that air damping is negligible compared to the intrinsic damping of the device. The internal or intrinsic damping is related to the device material, the method of fabrication and the dimensions of the device (length to thickness ratio, L/d). Since at low pressure the internal damping is dominated and independent of air pressure, the total damping is usually determined using empirical methods.

In the second pressure region, air damping becomes the dominant factor for the device. The density of the air is low so the air molecules are far apart and they do not interact with each other. In this case, the only interaction is between the individual molecules and the surface of the device. Thus, the damping is proportional to the air pressure and is also strongly influenced by the dimensions of the device.

In the third pressure region, the air molecules are close together so there is a strong interaction between them. In this case, air acts as a viscous fluid. Due to the fact that viscosity of the fluid is independent of the pressure, it can be assumed that the air damping is also independent of the pressure. In this pressure region if the device is close to another stationary surface, the region 3 damping is further increased because of the action of the air with the stationary surface. The space between the device and the stationary surface can be considered small when it is less then one third of the width of the device [Newell, 1968].

Because all simulations are conducted at a pressure level of 1 Pa ($10^5 N / m^2$), the third region of pressure is the most appropriate for our case as can be seen in Figure 12, where the air acts as a viscous fluid. In the next section, the equation of the air damping which is applied to the sensor is described based on the viscous fluid assumption.
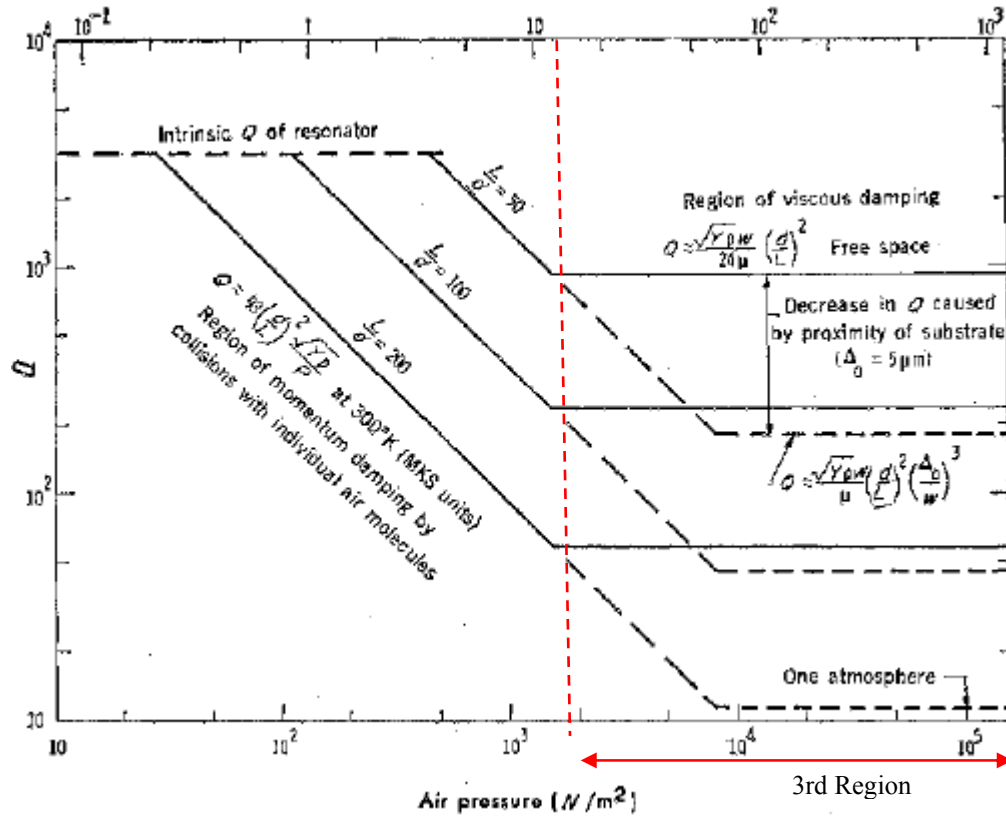
Figure 12. Variation of quality factor (Q)with Air Pressure for Resonators Having Various Length-to-Thickness Ratios (L/d) (After: Newell, 1968)

C. COMSOL SIMULATION PROCESS

For the primary sensor of the chip (# 8 sensor), as described in Chapter II, simulations were conducted using the COMSOL Multiphysics finite element modeling (FEM) program. COMSOL Multiphysics is a finite element analysis and solver software package for various physics and engineering applications, especially coupled phenomena, or multiphysics. A standard process is used in all the COMSOL simulation presented in this chapter. The basic steps of the process are the following:

1. Draw an object that will represent the actual design of the sensor
2. Assign the material from which the structure is made of.
3. Mesh the object.
4. Introduce the physics equations that will be used for the simulation.

5.   Establish the boundary conditions.

6.   Set the solver parameters.

7.   Run the simulation

Since the thickness of the sensor wings is fixed, a 2-D geometry of it was first drawn and then "extruded" to a 3-D object with a thickness of 10 microns. The 10-micron silicon layer is one of the two choices that the SOIMUMPs process allows. After the extrusion, the material type was set to "silicon".

After selecting the material, the meshing of the object becomes the next priority. The mesh procedure is a trade-off between the accuracy and the time it takes to run the simulation. If the device is meshed too finely, then the simulation will need a large amount of memory and the solution time will increase. At the other end, if the device is meshed too coarsely, results may be inaccurate. A compromise would make the meshing finer near the edges and in areas of small features, where detailed results are required, and make the meshing coarser in the other areas of the device. In any case, the quality of meshing is a factor that requires a serious consideration and a quite large number of trials to achieve good results.

Once the device is meshed, the physics equations that will be used for the simulation can be assigned, and boundary conditions can then be set. In our case, the entire device is free to move except for the two ends of the cantilever beams, which are fixed.

The next step is to set the program parameters and run the simulation. The analysis was concentrated on the frequency response of the sensor in the frequency range of the rocking (3-4 kHz) and bending modes (11-12 kHz) based on preliminary theoretical estimations using the dimensions and material parameters.

The equations and the parameters that are used for the simulation of the sensors with solid wings are listed in Table 2.

Parameter	Value	Description
μ	1.871e-5	Viscosity of the ambient air (Pa sec)
θ	Any value from 0 to 90	Incident angle (degrees)
ϕ	$\omega * \tau * \dfrac{180}{\pi}$	Phase difference (radians)
τ	$-x * \sin(\theta * \dfrac{\pi}{180}) \dfrac{1}{\upsilon_s}$	Time difference (sec)
Pda	$b\pi\sqrt{\dfrac{\rho\mu\omega}{2}}\upsilon_{z-direction}$	Formula computing air damping pressure [Zhang and Turner, 2004]
B	2	Empirical parameter [Zhang and Turner, 2004]
ρ	1.025	Ambient air density (Kg/ m^3)

Table 2.   Parameters Used for COMSOL Simulations

The formula in the Table 2 which describes the air damping is obtained from Zhang et al. [2006]. The damping coefficient, C_d can be estimated using the following relationship [Zhang and Turner, 2004]:

$$\frac{C_d}{unit\ length} = b * \lambda * \pi * \mu, \qquad (3.1)$$

where μ is the viscosity of air, $b \approx 2$ is an empirical parameter and λ is given by

$$\lambda = w\sqrt{\frac{\rho\omega}{2\mu}},$$

where ρ is the density of air and ω is the angular frequency of oscillations of the wings under the sound excitation.

According to Zhang and Turner (2004), the equation for the damping coefficient and the parameter b are applicable to devices with rectangular cross-section and thus valid in our simulation. Another consideration is the dependence of parameter b to the dimension of the structure that is parallel to the flow of fluid. For the device that is tested in this chapter, the parallel dimension is the thickness. The effect of the thickness in the simulation can be ignored, since the width-to-thickness ratio is relatively large [Zhang and Turner, 2004].

D. INTERPRETATION OF SOUND EFFECT ON THE SENSOR'S SURFACE

Assuming that the incident sound on the wings is a plane wave, the pressure at each point on the wings can be estimated using the phase change which depends on the incident angle. When the pressure wave is incident at some angle relative to the normal to the wings, the forces that are evolved have the same magnitude since the size of the sensor is much smaller than the wavelength of sound and only differ slightly in the phase. The phase difference is apparent, since when a plane wave such as the sound is incident on a surface at some angle, different points along the surface have different time of excitation. A trigonometric representation of the sound wave incident on the wings is given in Figure 13.
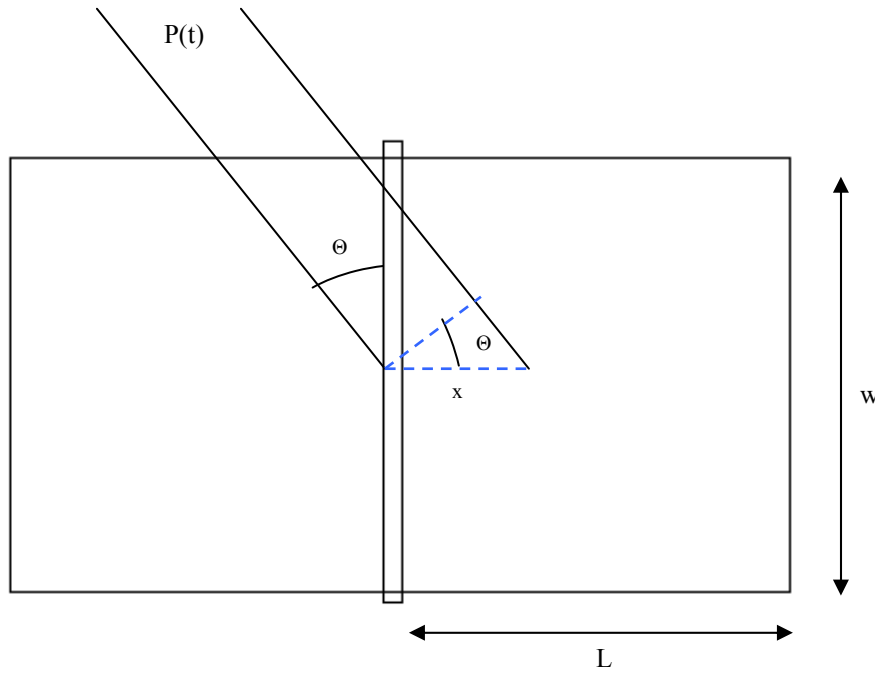
Figure 13. Representation of Sensor's Wings

The time difference of the force applied to each point of full device surface relative to the middle of the surface of the two wings (see Figure 13) is dependent on the distance from that point to the pivot point (x), the angle of the incident sound wave (θ) and the speed of sound (v_s). So, according to Figure 13, the time difference can be written as

$$\frac{x * \sin \theta}{\upsilon_s} \equiv \frac{dis\tan ce}{velocity}$$

The incident pressure at a distance x from the middle of the full device surface can be written as

$$P(t,x) = P_o * \cos\left[\omega\left(t - \frac{x * \sin \theta}{\upsilon_s}\right)\right] \qquad (3.2)$$

where the parameters of its equation are the following:

- P_o , the magnitude of the Pressure of the sound wave (Pa).

- ω , the angular frequency (Hz).

- υ_s , the speed of sound (344 m/sec).

- θ , the incident angle of the sound plane wave (degrees).

Equation 3.2 can be easily implemented in COMSOL to determine the response of the sensor.

An incident acoustic pressure wave is applied to the wings of the sensor in a continuous distributed force field. According to the following derivation, this force can be represented as two point forces, each applied at the center of each wing. This simplification is necessary in order to use the mechanical model described in Chapter I for the simulation. When the wave is incident at some angle relative to the sensor's longitudinal axis, these two point forces will differ slightly in the phase. These forces have the same amplitudes due to the relatively short distance between their points of application compared to a sound wavelength with frequency in the 3-4 kHz range.

The force on the wing on the right can be obtained by integrating the pressure over the area of the wing as:

$$\mathrm{F} = \int_0^L w * P(t,x)\, dx \qquad (3.3)$$

where w is the width of the wing of the sensor, L is the length of each wing, x, is the coordinate of the point along the axis of the sensor's wings.

Substituting equation (1.1) into (1.2), the applied force is calculated as follows:

$$F = \int_0^L w * P_o * \cos\left[\omega\left(t - \frac{x*\sin\theta}{\upsilon_s}\right)\right] dx. \tag{3.4}$$

In order to solve the above integral, we take into account the trigonometric formula:

$$\cos(\alpha - \beta) = \cos\alpha * \cos\beta + \sin\alpha * \sin\beta. \tag{3.5}$$

Combining (3.4) and (3.5) gives

$$F = w * P_o \int_0^L \left[\cos(\omega*t)\cos\left(\frac{\omega*\sin\theta}{\upsilon_s} * x\right) + \sin(\omega*t)\sin\left(\frac{\omega*\sin\theta}{\upsilon_s} * x\right)\right] dx$$

$$= w * P_o * \left[\cos(\omega*t) * \frac{\upsilon_s}{\omega*\sin\theta} * \sin\left(\frac{\omega*\sin\theta}{\upsilon_s} * L\right) - \sin(\omega*t) * \frac{\upsilon_s}{\omega*\sin\theta} * \left[\cos\left(\frac{\omega*\sin\theta}{\upsilon_s} * L\right) - 1\right]\right]$$

$$F = 2 * w * P_o * \frac{\upsilon_s}{\omega*\sin\theta} * \sin\left(\frac{\omega*\sin\theta}{\upsilon_s} * \frac{L}{2}\right)\left[\cos(\omega*t)\cos\left(\frac{\omega*\sin\theta}{\upsilon_s} * \frac{L}{2}\right) + \sin(\omega*t)\sin\left(\frac{\omega*\sin\theta}{\upsilon_s} * \frac{L}{2}\right)\right]$$

$$= 2 * w * P_o * \frac{\upsilon_s}{\omega*\sin\theta} * \sin\left(\frac{\omega*\sin\theta}{\upsilon_s} * \frac{L}{2}\right)\cos\left(\omega*t - \frac{\omega*\sin\theta}{\upsilon_s} * \frac{L}{2}\right). \tag{3.6}$$

Because the factor $\dfrac{\omega*\sin\theta}{\upsilon_s} * \dfrac{L}{2}$ can be regarded as very small, the following approximation may be used:

$$\sin\left(\frac{\omega*\sin\theta}{\upsilon_s} * \frac{L}{2}\right) \approx \frac{\omega*\sin\theta}{\upsilon_s} * \frac{L}{2}. \tag{3.7}$$

Using Equation 3.7, Equation 3.6 can be expressed as,

$$F \approx w * P_o * L * \cos\left(\omega*t - \frac{\omega*\sin\theta}{\upsilon_s} * \frac{L}{2}\right) \Rightarrow P \approx P_o * \cos\left(\omega*t - \frac{\omega*\sin\theta}{\upsilon_s} * \frac{L}{2}\right). \tag{3.8}$$

From Equation 3.8 it is seen that that the incident pressure wave can be represented by two point forces with amplitude given by the product of the acoustic pressure and the wing's surface area. Assuming that the direction of the propagation of

24

the incident wave is at an angle θ relative to the device's longitudinal axis, then the phase difference between the left and right wing (ipsilateral and contralateral) from the pivotal point is $\pm \dfrac{\omega * \sin \theta}{\upsilon_s} * \dfrac{L}{2}$, respectively.

E.   COMSOL SIMULATION RESULTS

Table 3 shows the simulated results for sensor #8, which has solid wings using COMSOL for a number of different incident angles of sound. The displacements of the left and right wing (ipsilateral and contralateral) for rocking and bending modes as well as the frequencies at which each mode occurs can be seen in the Table 3. All simulations are executed with intensity of sound wave of 1 Pa and with a damping force calculated by Equation 3.1.

Incident Angle	Frequency		Displacement Ipsilateral Wing		Displacement Contralateral Wing	
	Rocking Mode (kHz)	Bending Mode (kHz)	Rocking Mode (nm)	Bending Mode (nm)	Rocking Mode (nm)	Bending Mode (nm)
15°	3.48	11.11	268	4273	238	4267
30°	3.48	11.11	505	4265	475	4258
40°	3.48	11.11	642	4251	612	4258
45°	3.48	11.11	705	4254	675	4247
55°	3.48	11.11	785	4247	815	4239
70°	3.48	11.11	930	4237	900	4229
90°	3.48	11.11	990	4232	960	4224

Table 3.   COMSOL Simulations for Device No 8

The displacements of left and right wings (ipsilateral and contralateral) as a function of the incident angle for the rocking and bending modes are depicted in Figures 14 and 15, respectively, using the data of Table 3. It can be seen that, as expected, the amplitude of the rocking motion rapidly increases as the angle increases, while the amplitude remains nearly the same for the bending motion.
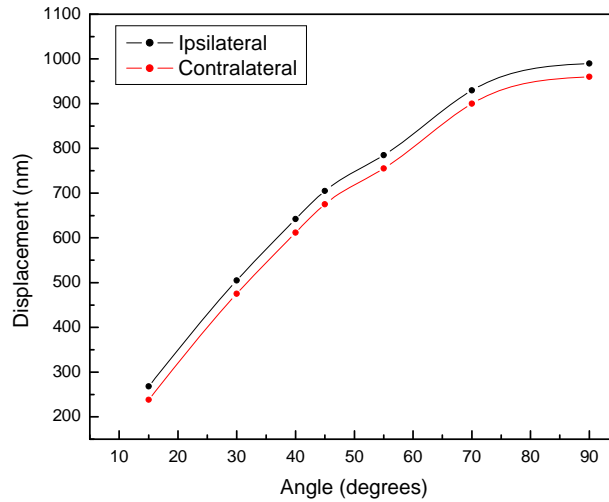
Figure 14.   Displacement in Rocking Motion versus Angle of Incidence
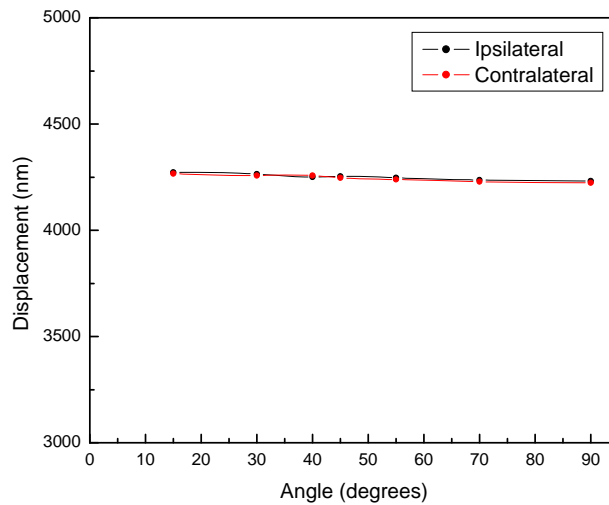
Figure 15.   Displacement in Bending Motion versus Angle of Incidence

The rocking mode of the device resembles a seesaw motion as it rocks back and forth. Figure 16 shows the 3-D view of the device in the pure rocking mode while Figure 17 shows the device in the pure bending mode.
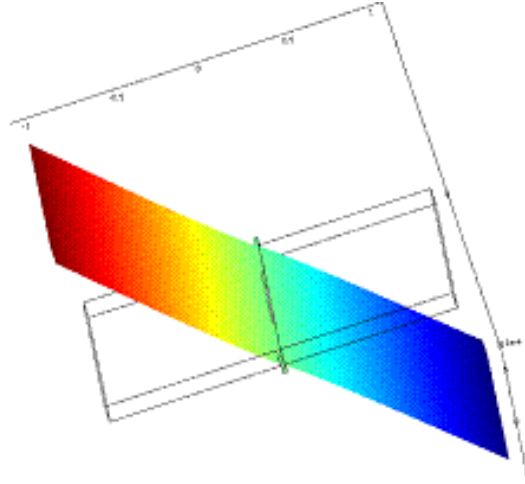
Figure 16.   Device in Pure Rocking Mode

An animation of the sensor's motion using COMSOL simulation package. The seesaw motion of the sensor in the rocking mode is apparent.
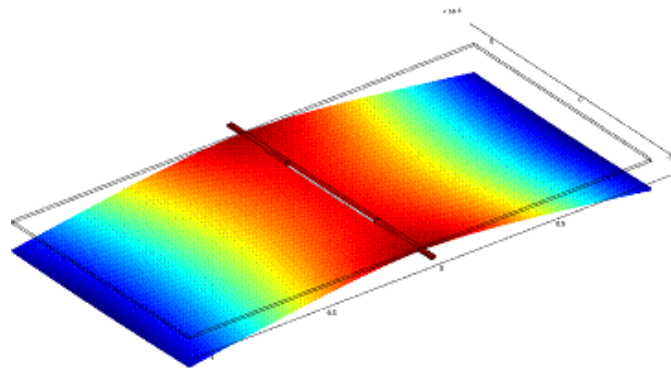
Figure 17.   Device in Pure Bending Mode

An animation of the sensor's motion using COMSOL simulation package. Motion in the bending mode looks like a bird flapping its wings in flight.

Pure rocking or bending motions occur only at the respective frequencies. In all other frequencies a combination of those two modes arises, with different contribution from each mode depending on the frequency. It is important to note that the initial

27

condition of the system (i.e., the incident angle) also affects the motion of the device. For example, normal incident sound excites only the bending motion regardless of the frequency of the incident sound wave. Typically a linear combination of the two modes (rocking and bending) occurs simultaneously. The displacements due to these modes add together at the left (ipsilateral) wing while in the right (contralateral), these two subtract from each other creating smaller amplitude motion. The overall result is a difference in the two wings' amplitudes depending on the initial conditions of the system. A detailed analytical derivation of the equations of motion and of the linear combination of the modes can be found in Miles, Robert and Hoy [1995]. In Figure 18, a 3-D view representation of the motion of the device is shown, for 45º incident angles and at a frequency of about 3.8 kHz.
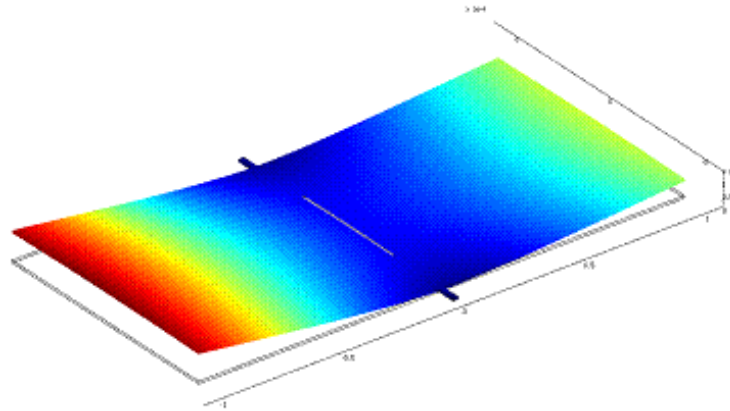
Figure 18.　　Device in Vibration at 3.8 kHz

An animation of the sensor's motion using COMSOL simulation package. It can be observed that in a frequency between the rocking and bending mode a combination of the two distinct motions is occur.

IV. CHARACTERIZATION OF SENSORS

A. INTRODUCTION

The measurement of sensor performance includes the determination of vibration amplitudes of the two sensor wings in relation to sound frequency, pressure and angle of incidence. The vibrational amplitudes are measured using a laser vibrometer, which can monitor vibration amplitudes down to picometer range. In the following sections, the experimental design used to test the MEMS sensor is described.

B. INSTRUMENTATION

Figure 19 is a photograph of the laboratory setup that was used to measure the amplitudes of the sensor vibrations.
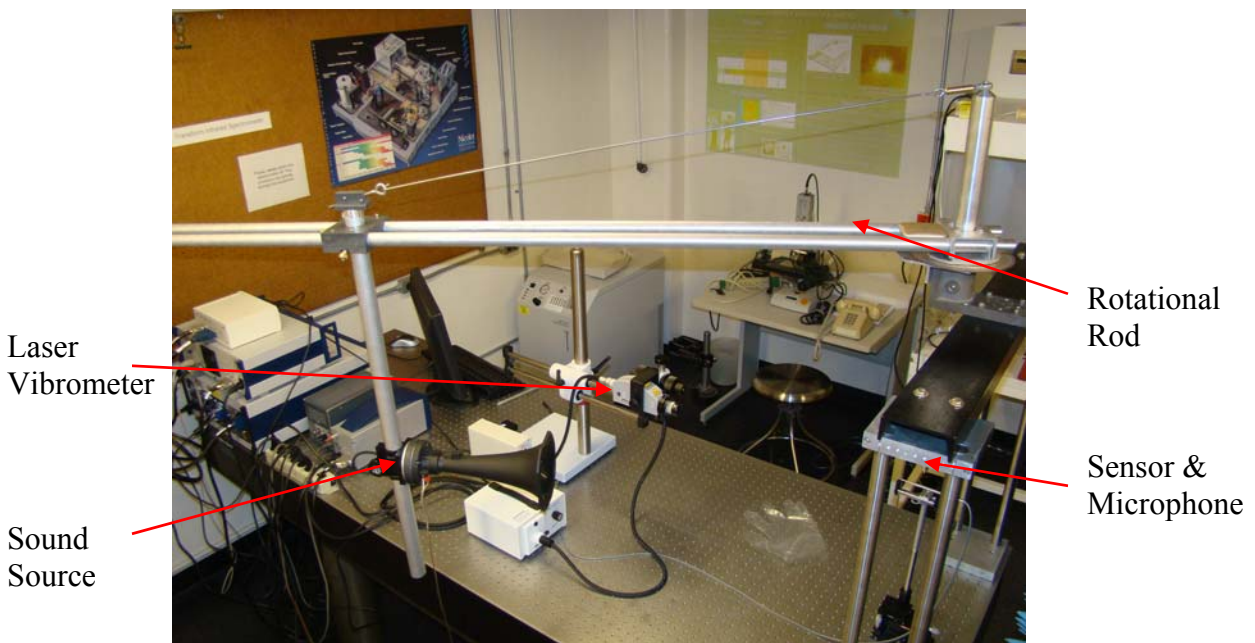
Figure 19.   Equipment in Lab Used During the Experiment

The basic components used for the testing of the sound sensor are the reference microphone (for measuring the sound pressure), the sound source, the laser vibrometer and, finally, the chip containing the sensors.

The reference microphone, used to measure the sound pressure near the tested device, is placed just above the chip containing the sensor, as shown in Figure 20.
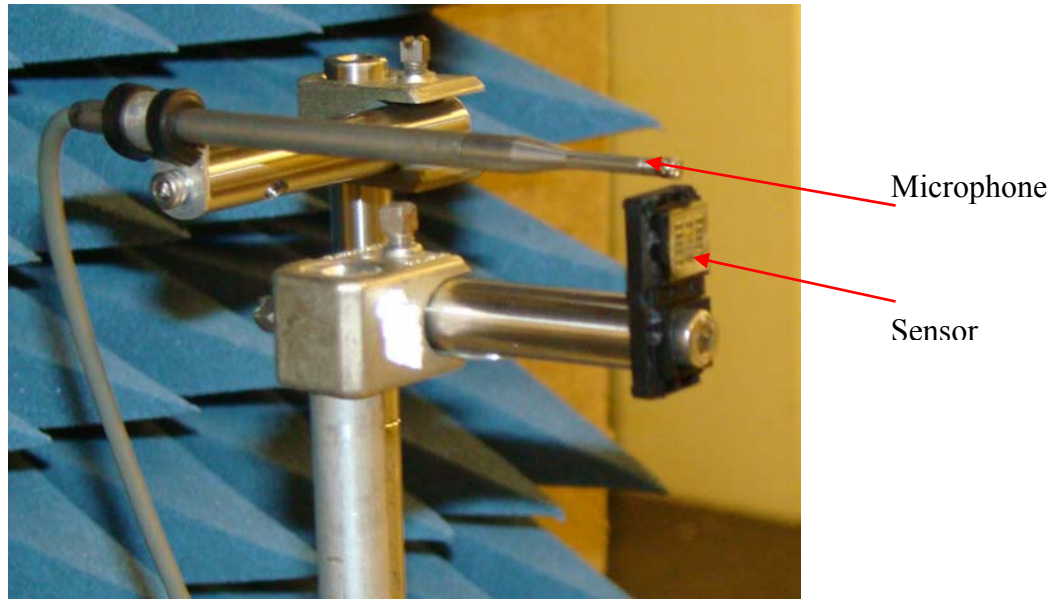
Figure 20.   Sensor and Microphone Used in the Experiment

A Bruel & Kjaer® model 4138 1/8-inch microphone [Bruel & Kjaer, 1989] is used to measure the sound-pressure response. This microphone was chosen due to its small size and its high sensitivity relative to its dimensions. It has a frequency response that is almost flat from 50 Hz to 20 kHz, as shown in Figure 21.
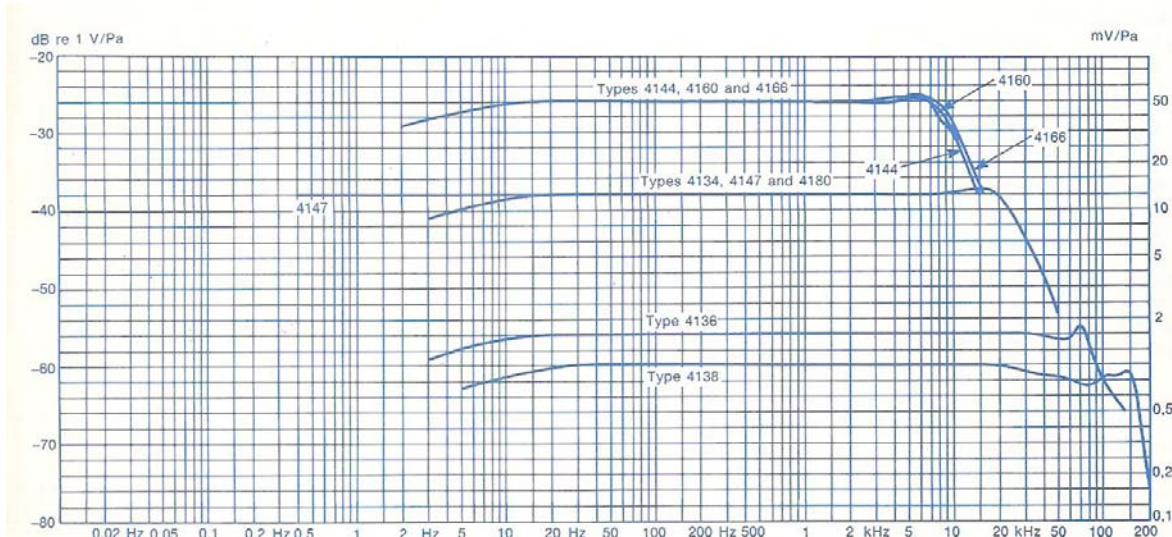
Figure 21.   Frequency Response of Bruel & Kjaer Microphones (From: Bruel & Kjaer, 1989)

Another important factor in the selection of a microphone is the effect of free-field corrections. Free-field corrections represent the increase in sound pressure caused by diffraction of the sound wave around the head of the microphone. These are considered to be significant at high frequencies, where the wavelength of the sound is comparable to the dimensions of the microphone. Correction curves for diverse angles of incidence can be seen in Figure 22. It can be seen that the corrections are small and can be considered negligible in the range of frequencies (1-12 kHz) that the sensor is designed to operate.
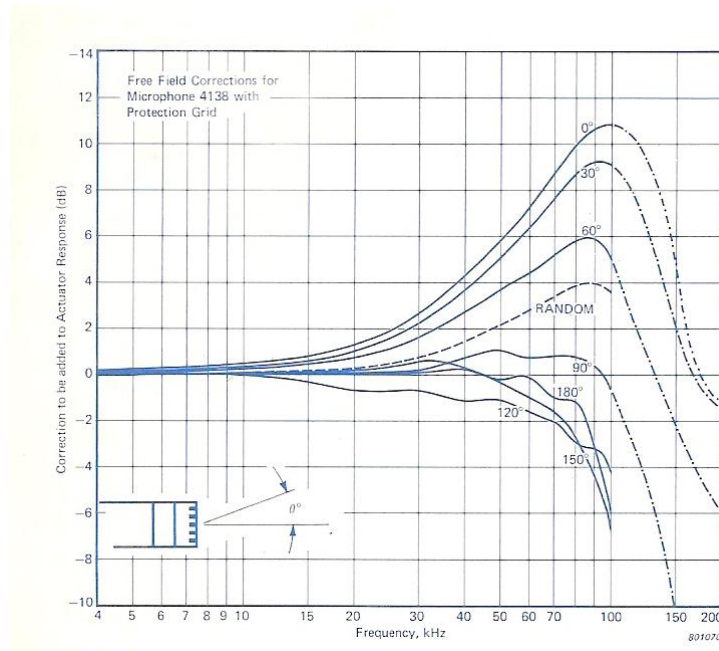
Figure 22.   Free-Field Correction Curves for Various Angles of Incidence (From: Bruel & Kjaer, 1989)

The sound source is a Selenium loudspeaker type DH200E connected to a Hewlett Packard® (HP) 467A power amplifier. This setup is used to generate sound waves with different amplitudes and frequencies for assessing the sensor performance. The output characteristics of the speaker are shown in Figure 23.
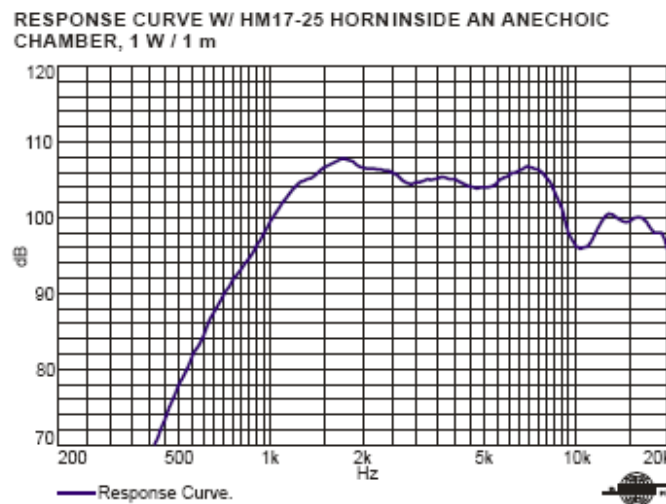
Figure 23.   Response Curve for Loudspeaker DH-200E(From: Leiritronica, 2008)

The incident angle of the sound wave is altered manually by moving the rotational rod shown in Figure 19. A protractor is attached to the apparatus to allow for precise reading of the rod angle.

The laser vibrometer head is a Polytec® model OFV-534 coupled with a model OFV-5000 controller. The purpose of these devices is to measure the displacement of the wings of the sound sensor with precision on the order of tens of picometers. In addition, the vibrometer controller provides waveforms for driving the speaker. The waveforms include single frequency as well as periodic chirp for measuring the frequency response. In the following table, basic specifications of the vibrometer can be seen as described in the User Manual [Polytec, 2007] of vibrometer sensor head OFV-534.

Laser Type	Helium Neon
Wavelength	633nm
Laser power	< 1Mw
Cavity length	204mm+/- 1mm
Ambient Conditions	
Operating Temperature	+5°C to +40°C (41°F to104°F)
Storage Temperature	-10°C to +65°C (14°F to149°F)
Relative Humidity	Maximum of 80%

Table 4.   Technical Specifications of Vibrometer OFV- 534 (From: Polytec User
              Manual, 2007)

The experimental runs were conducted at an ambient air temperature of about 70°F, which is well within the operating range of the laser vibrometer. A video camera attached to the vibrometer head provides a real time image of the sensor chip along with the location of the laser spot. This allows for easy positioning of the laser beam on the point of the surface of the wing where the vibration are measured.

There is a close relationship between the standoff distance (between the vibrometer and the sensor) and the spot diameter (see Table 2) of the laser beam that is created on the surface of the sensor chip. It is desirable to have a large standoff distance between the laser vibrometer and sensor chip to minimize the scattering of sound from it. However, this leads to an undesirable effect of increasing the laser spot diameter.

The standoff distances (measured from the front of the sensor) and the corresponding spot diameters (without using the microscope lens attached to the laser vibrometer) available with the OFV-534 are given in Table 5.

Stand-off Distance (mm)	Spot Diameter (microns)
200	25
400	56
600	86
1000	148
1500	224
2000	302

Table 5.   Standard Characteristics of the Laser Vibrometer OFV- 534 (From: Polytec User Manual, 2007)

Figure 24 shows a photograph of the chip and all its sensors, as captured from the camera of the vibrometer.

Individual sensors inside the chip
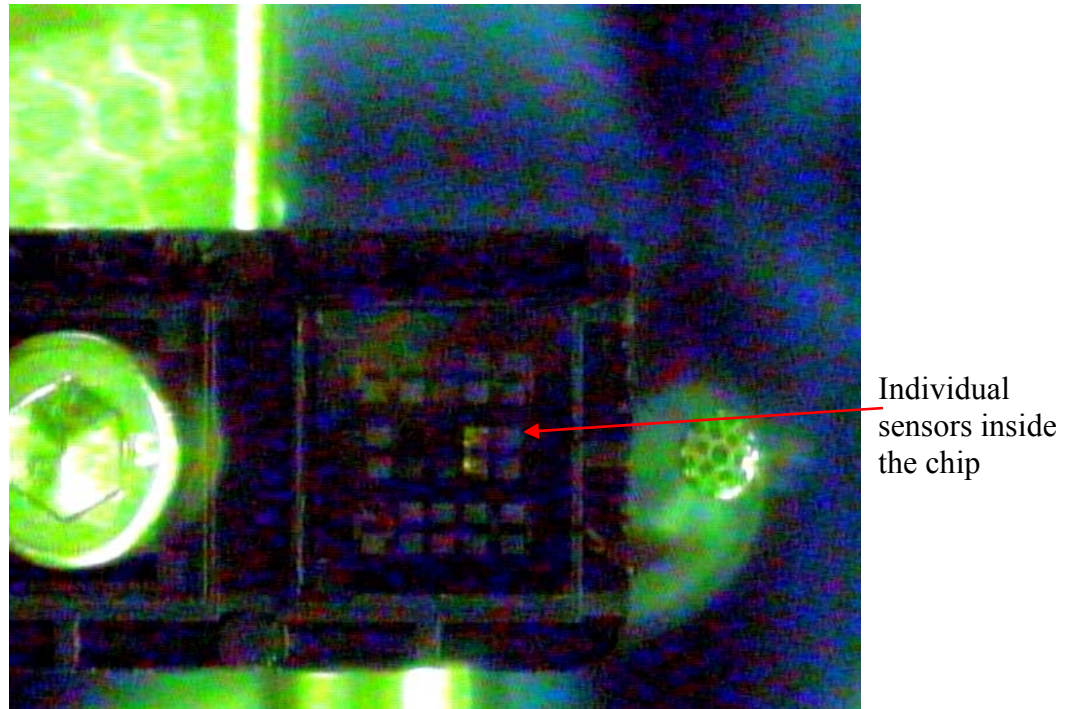
Figure 24.   Photo of the Chip from the Laser Vibrometer

In addition to the hardware, the Polytec vibrometer is equipped with versatile software for data acquisition and generation of waveforms for driving the speaker. The basic functions operated through the software are:

- Setting the optics, controlling the camera and the focus of the laser.

- Setting the parameters of data acquisition, controlling parameters in regard with the frequency, filters, generator (loudspeaker), trigger, vibrometer, other secondary channels (reference microphone) and finally the signal enhancement.

- Taking the measurements.

C.   EXPERIMENTAL DESIGN

The main goal of this experiment is to describe the relationship between a set of experimental factors (predictor variables) and the positional displacement of the wing of the MEMS sensor (outcome variable).   The experimental factors represent varying conditions under which sound is projected towards the sensor.

35

The goal of this experiment is to estimate the response (outcome) variable (Y), which represents the amplitude of the vibration of the sensor's wing. Y is measured in nanometers. The independent (predictor) variables are the following:

- Incident angle (X_1) measured in degrees at levels 10,25,40 and 60

- Intensity of the sound (X_2) measured in Pa at levels 0.2, 0.4 and 0.6

- Frequency of the sound wave (X_3) measured in Hz at levels 2600, 2800, 3000, 3200 and 3400

- Identification of the two identical, tested devices, using the categorical variable X_4, with values 0 or 1.

A general formulation of the model is $Y = g(X_1, X_2, X_3, X_4, \varepsilon)$, where ε is a random error term. In Chapter V, the specific form of this model is explored using data analysis. A more detailed justification of the factors and the levels of them will be presented later in this chapter.

1.   General Considerations

An important part of statistical analysis is the manner in which data are collected. Some of the basic methods for collecting data are the following:

- A study based on historical data.
- An observational study.
- A designed experiment.

The data collection method for this study is a designed experiment where a set of variables (factors) are set at different levels. In order to conduct a factorial experiment, each combination of factor levels is observed at least once. If each combination is observed the same number of times, the experiment is said to be balanced. For example, if there are l_1 levels for the first factor, l_2 levels for the second factor, and so forth with l_k the number of levels for the kth factor. If every treatment combination is observed exactly once, the total number of experimental runs would be $l_1 \times l_2 \times l_3 \times \cdots \times l_k$. In many situations the factors are continuous variables that are observed at pre-specified values, in which case there is a tradeoff between the extent of discretization and the number of

experimental runs required. In the case of a small number of levels (2 or 3), this design requires a relatively small number of treatment combinations. Although it is difficult to explore precisely the response variable in relation to the factor space with a sparse design of this type, it can indicate major trends and determine the right direction for further experimentation. Figure 7 illustrates the implementation of a factorial type of design in this study. In this case, a cube is formed where each major axis represents a factor of the design, and along each axis there are the corresponding levels of the factors.
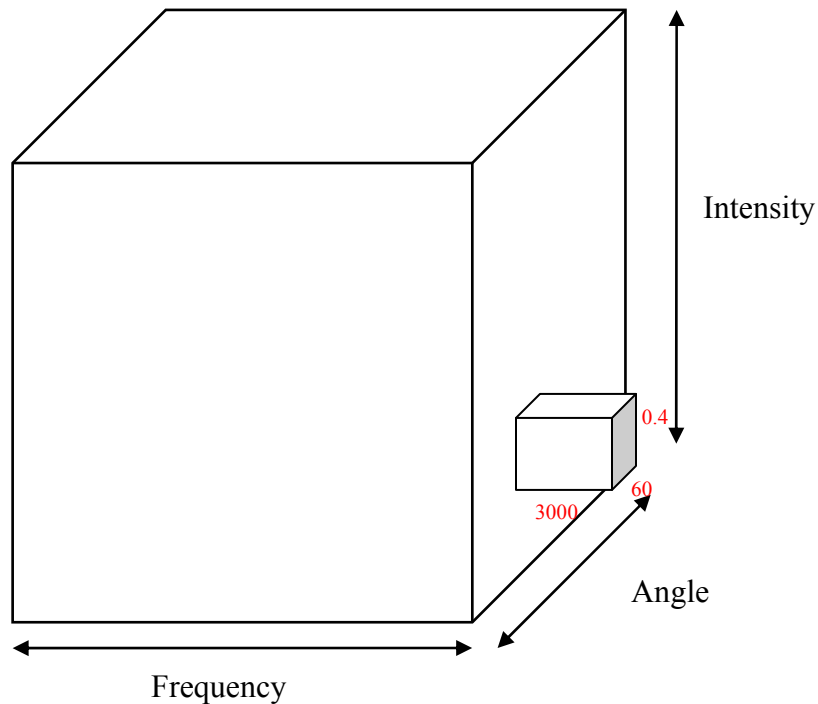
Figure 25.   Factorial Design

        Geometric representation of the experimental factors and the different levels they are set at. The large cube represents all the combined experimental runs (60 in total). The smaller cube represents one experimental run, for Angle 25, Intensity 0.4 and Frequency 3000.

In Figure 25, the three axes represent the three factors (Frequency, Angle and Intensity) that will be investigated in the sound sensor and that will be explained thoroughly later in this chapter.

A factorial design allows detecting and estimating interactions between the factors that account for nonadditive behavior. Less costly designs in which factors are not completely crossed with each other afford less flexibility in this respect. Such an experimental method is superior to one which would allow for only one factor to vary at a time, while the remaining factors would be held constant. In such a case, a generalization of the effect of the varying factor would require an assumption that the effects of this factor would be the same even at different levels of the constant factors. Such an assumption could be misleading if there are, in fact, interactions between some factors.

2.   Selection of Factor Levels

At this point of the study, the basic problem of the experimental design is to decide what pattern of design points will best reveal aspects of the situation of interest which in this case is the response of the sensor. Points on a diagram as illustrated in Figure 26 can represent the runs that the experimenter decides to conduct.
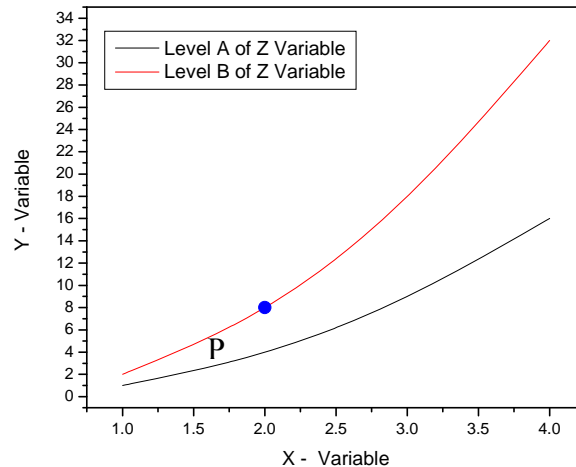
Figure 26.   Representation of Relationship between Two Variables Stratified by a Third Variable

The point labeled P represents a potential experimental run at X=2 and Z at level A.

In Figure 26, one quantitative factor (*X*) and one categorical factor (*Z*) are represented. The point labeled P represents a potential experimental run at $X = 2$ and *Z* at level A. The response variable is observed to be $Y = 8$. Ideally, the selection of design points is made to allow the form of the response function to be identified as accurately as possible for a given number of experimental runs. It is important in designing an experiment to use any known scientific principles about the problem that is being investigated.

Factorial designs facilitate the discovery of similarities and simplifications which are important for model building. These experimental designs can also provide estimates of the effects of the changes, assuring simultaneously that the experimental error is kept as low as possible.

D.   MEASUREMENTS AND CONSIDERATIONS BEFORE THE INITIATION OF THE EXPERIMENT

In an experiment, decisions must be made on the factor levels that will be used. Some of the considerations that are taken into account in this study are the following:

- Which variables are the most important to evaluate and describing the response function?

- Over what range should the variables should be studied?

- How many factor levels should be used for each variable, and what should they be?

- In what scale should the analysis of the response variable be conducted (linear or logarithmic)?

In order to identify a stable and reliable setup of the experiment, a number of trial measurements were made. It was found that some of the parameters needed to be modified during the conduct of the experiment, which include the following:

- The position of the sound source was elevated in order to eliminate the reflections of the sound on the surface of the table;

- A hone was attached to the sound source in order to increase the directionality of the sound;

- Absorbing material was used to minimize the reflections of the sound from the walls and the other structures inside the lab;

- Data were collected in both frequency and time domains;

- The values of the displacement of the wing of the sensors as well as the normalized values (using the reference microphone) were to be collected;

- The spot of the laser beam was kept relatively small in order to facilitate the experimenter, to aim the laser at the edges of the wings of the sensor where the amplitude is the largest. The laser vibrometer was positioned at a stand off distance from the sensor of around 57 cm resulting in a spot at the surface of the sensor of about 80 microns diameter.

As shown in Figure 27, the resulting design contains all combinations of the determined levels for all of the quantitative factors (Intensity, Angle, and Frequency).
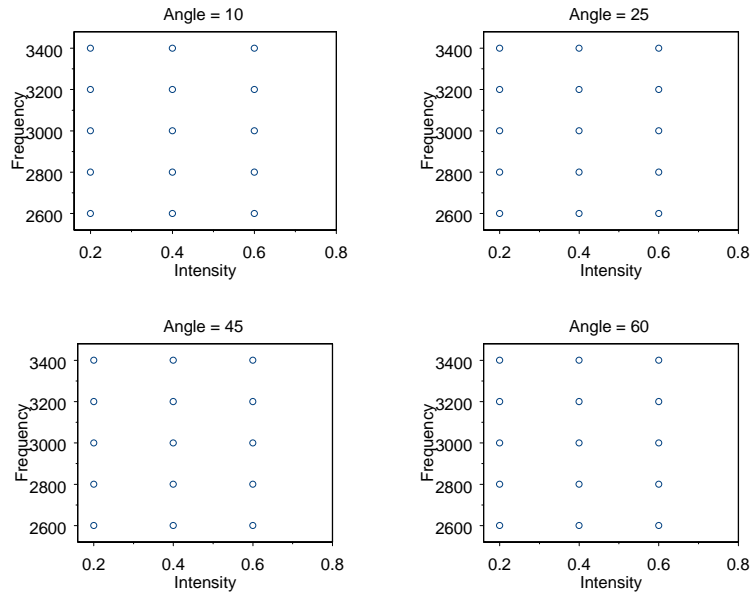
Figure 27.   Factorial Arrangement of Experimental Runs

Graphical representation of all the experimental factors and all the different combinations of levels they are set at. Each point on the graph represents an experimental run. There are 4 levels of Angle represented by different subfigure with 5 levels of frequency and 3 levels of Intensity. All the combinations of these levels produce a total of 60 experimental runs for each of the two sensors.

Intensity is described by three levels, 0.2, 0.4 and 0.6 Volts based on the control voltage applied to the amplifier. The amplifier generates an output voltage depending on the gain used to drive the sound source. The signal from the reference microphone was converted to pressure using its conversion factor of approximately 1 V/Pa. In order to determine the intrinsic noise of the sensor the vibration amplitudes were measured without turning the speaker on. Under these conditions, the vibrations are primarily due to background sound in the lab as well as thermal agitations. The magnitude of this vibration (intrinsic noise) was of the order of 0.01 nm while the displacement of the wing for 0.1 Pa intensity of sound was on the order of 1 nm. In order to assure that the intrinsic noise level would be negligible, the minimum intensity of the sound wave was set to 0.2 Pa. The upper level of the intensity was limited by the fact that intensities approaching 1 Pa could be harmful to the experimenter.

The next factor of the experiment was the frequency of the sound. As described in previous chapters, the designed rocking frequency of the sensor was approximately at 3400 Hz. In addition to this, experimental trials were conducted to determine the actual rocking frequency which turned out to be around 3000 Hz, as can be seen in Figure 28. So another 4 levels of frequency were established in order to describe the decay ratio of the amplitude, away from the resonance frequency (3000 Hz). These four levels were settled in two steps of +/-200 Hz from the designed frequency.
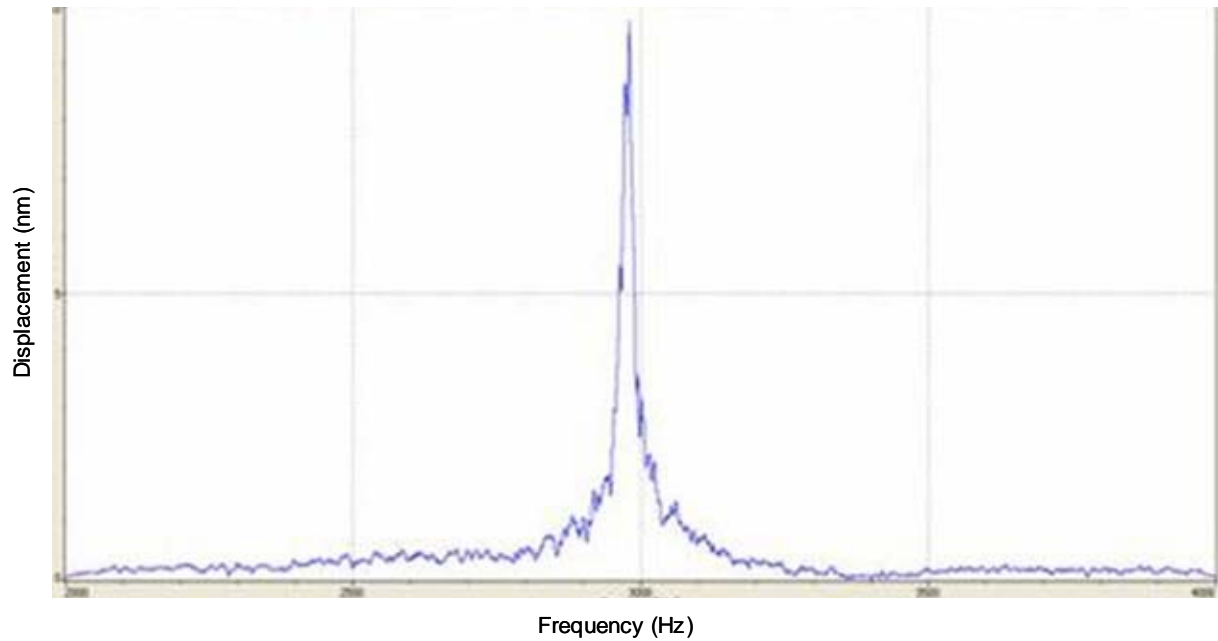
Figure 28.   Frequency Response of the Sensor about the Resonant Rocking Frequency

The third factor is the Angle of Incidence with four levels (10, 25, 45, and 60 degrees, measured as departures from the normal of the sensor's surface). The reliability of measurements for angles greater than 60 degrees was doubtful mainly because of the masking of the sound by the posts that hold the speaker and the multiple reflections that occur in those angles.

In Appendix A the combinations of all levels is presented, considering that the final arrangement of the experiment was consisted from 4 (Angle) × 3(Intensity) × 5 (Frequency) × 2 (Device), giving a total of 120 experimental runs.

Two identical sensor units were obtained from the manufacturer, and tested to detect inter-unit differences. In the experiment, the dichotomous (0 or 1) variable "Device" is introduced to distinguish these units.

V. DEVICE TESTING

A. INTRODUCTION

With the existence of the rocking and bending modes of the biomimetic sensor having been established through the simulations discussed in Chapter V, the next phase of the research is to test the fabricated devices in a sound field. For these tests, two identically fabricated MEMS chips are studied. On each chip, 15 different devices, each with a different design, were placed for testing purposes. Chip layout is discussed in more detail in Chapter II of this thesis.

The testing starts on the sensor on the first chip having solid wings (Device #11). Later in the process, the second chip is used to further analyze the performance of two identical devices (# 8 and #11) with solid wings. Finally, Device #10, with perforated holes in the wings, is tested in order to determine the effects of such holes on the sensor.

B. FREQUENCY RESPONSE OF DEVICE # 11 OF THE FIRST CHIP

It was decided that Device #11 would be tested first because this device had the best simulated results (maximum vibration amplitude) using COMSOL software. The sound frequency region of interest is 2 to 14 kHz, since the simulated rocking and bending modes of the device occurred at 3.5 kHz and 11.5 kHz, respectively. Figure 29 shows the distinct rocking and bending modes during the testing of the device in the sound field. The rocking frequency of the device is measured to be around 3 kHz, while the bending mode is around 11.4 kHz. The procedure used to collect the data includes the following design parameters:

- A sound frequency bandwidth equal to 20 kHz was applied;

- Reduction of the noise bandwidth was achieved with band-pass filtering to retain frequencies from 2 to 14 kHz;

- Response was represented in fast Fourier transform (FFT) mode with 12800 lines in order to increase the accuracy of the measured sensor's response;

- Sound pressure was applied using a periodic chirp (from 2 to 14 kHz) of 1 Pa.
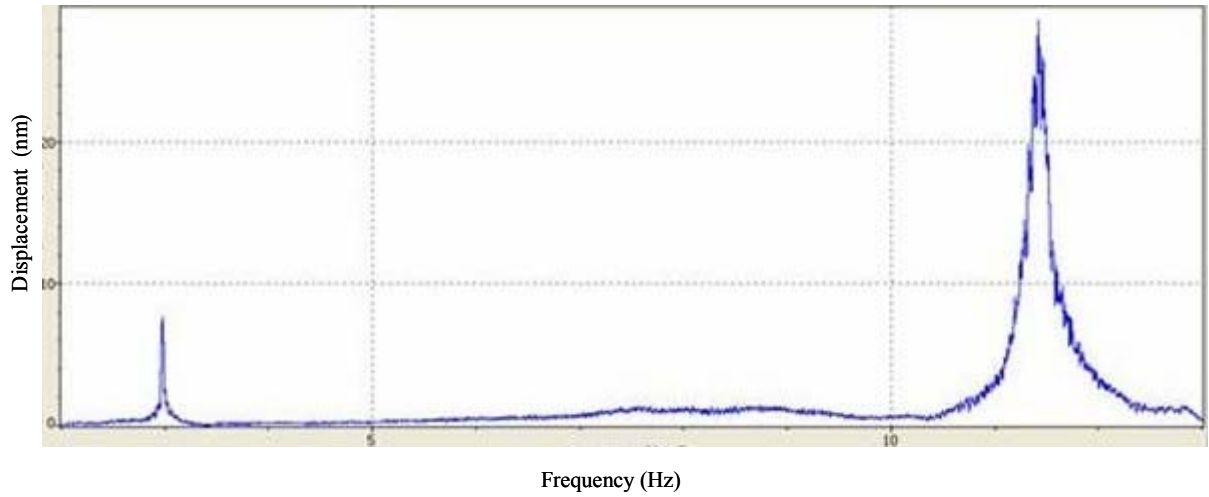
Figure 29.   Frequency Scan of the Sensor Tested using Sound
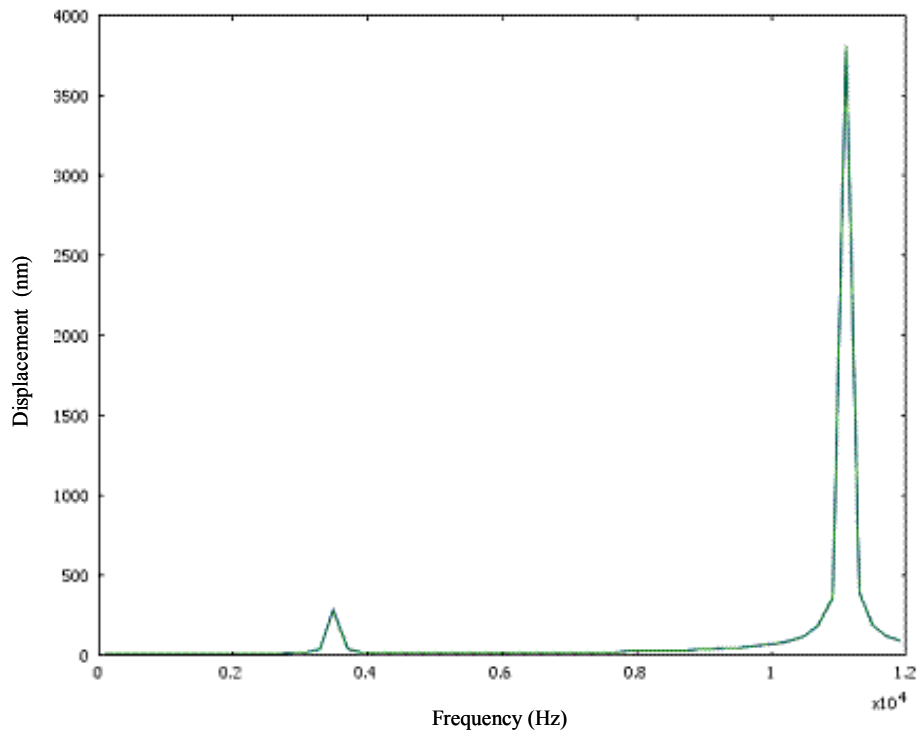
Figure 30.   Simulated Frequency Response of the Sensor #11 using COMSOL

Figure 30 represents the simulated frequency response of the device using the simulation program COMSOL. The Device #11 simulation shows two distinct peaks, one for the rocking mode at 3.4 kHz and the other for the bending mode at 11.4 kHz, both with sharp profiles. The bending mode appears to coincide with the experimental data at a frequency around 11.5 kHz while the rocking frequency is about 400 Hz greater (3400 Hz).

At this point, it is important to determine how some of the design parameters affect the value of the rocking frequency of the sensor. The spring constant of the device, K_s, is defined as the ratio of the applied force, F, on the device and its resultant displacement, x:

$$K_s = \frac{F}{x}.$$

The rocking motion is due to the torsion of the two beams that connect the wings to the substrate. The corresponding spring constant depends on the dimensions of the beam and has the form

$$K_s \propto \frac{wt^3}{l^3} \tag{5.1}$$

where w is the width, t is the thickness and l is the length of the beam [Liu, 2006]. The spring constant decreases with increasing length, increases with increasing width and is strongly influenced by the change in the thickness due to the presence of the term t^3.

Also, the mass of the wings is proportional to its thickness, which gives

$$m \propto t. \tag{5.2}$$

From Equations 5.1 and 5.2, it can be derived that $\frac{K_s}{m} \propto t^2$.

Since $\omega_{Rocking} = \sqrt{\frac{K_s}{m}}$, it leads to $\omega_{Rocking} \propto t$. So due to the proportionality of rocking frequency and the thickness of the device, a 10 percent decrease of thickness should cause a 10 percent decrease of the rocking frequency. Thus, it is possible that the difference between the experimental and simulated data may be due to variation in the thickness of the SOI device layer, which is present in the experimental data but not in the

45

simulation. Such variation is within the specifications given by the manufacturer, since the variation of silicon thickness is estimated +/- 1 micron [Miller et al., 2004]. In the next section, a set of additional simulations that were conducted to investigate the behavior of the sensor with a hypothetical thickness of 9 microns is described.

C.   REVISED COMSOL SIMULATION RESULTS

In order to investigate the observed difference in the simulated and experimental data of the rocking frequency of the sensor, another set of simulations is carried out by varying the thickness of the SOI layer. Special consideration is given to the level of meshing that is used during the revised simulations. The level of meshing is a factor that describes the accuracy of the simulated output data. As was mentioned in an earlier chapter, the mesh procedure is closely related to the time it takes to run a simulation. In the new simulations, a mesh with twice the level of refinement is used to acquire more precise measurements. Also, the thickness of the sensor wings is reduced from 10 to 9 microns to observe the effects on the rocking frequency.

Figure 31 shows the simulated frequency response of the device with the altered parameters as obtained from COMSOL. The rocking mode is now shifted to the left at a frequency of around $0.31 \times 10^4 \, \text{Hz}$.
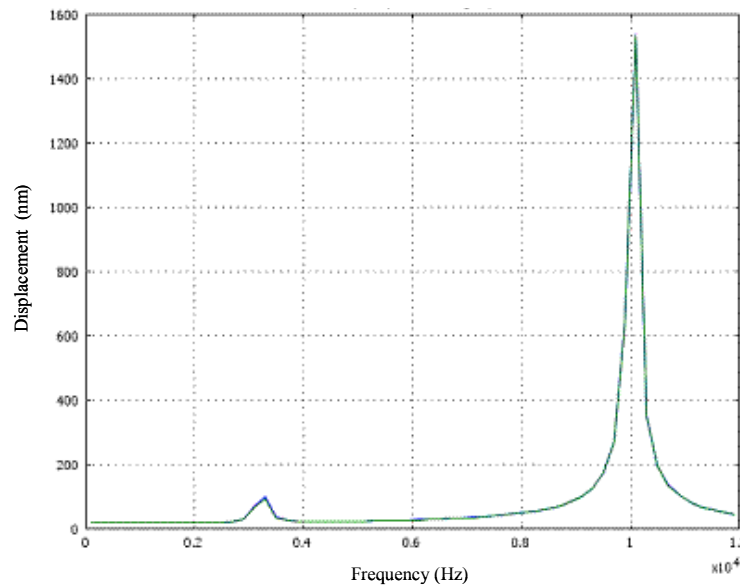
Figure 31.   Frequency Response of the Sensor Simulated using COMSOL

The results of the revised simulations support a finding that a decrease in the sensor's thickness can result in a similar decrease of the rocking frequency on a relative scale. This suggests that the difference in rocking frequencies between the experimental and simulated data may be attributed to variations from the tolerance limits of the SOI layer thickness as specified in the SOI manual [Miller et al., 2004].

Further simulations are then conducted to measure the displacement of the wings of the sensor (both left and right) with respect to the incident angle of the sound wave. Figures 32 and 33 illustrate the displacement of the sensor's wings at various incident angles for the rocking and the bending modes, respectively. Consistent with the mechanical model discussed in Chapter I, the amplitude of the bending mode remains nearly constant as the incident angle is varied. However, the amplitude of the rocking mode is strongly dependent on the incident angle.
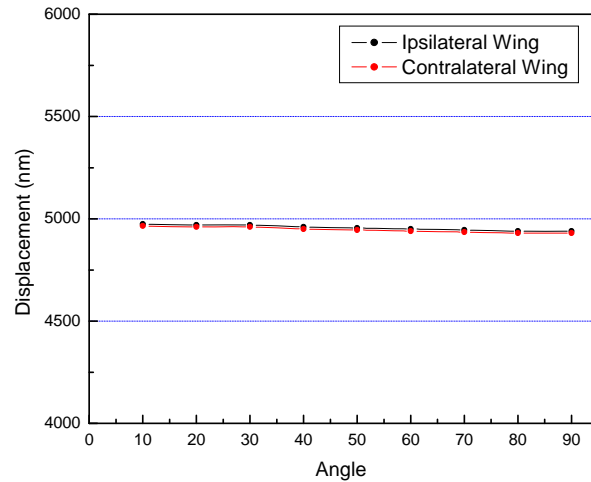
Figure 32.   Amplitudes of Bending Motion of the two Wings versus Incident Sound Angle

The amplitudes of both wings of the sensor have the same magnitude and are independent of the incident angle of sound as they remain nearly constant for various angles (almost horizontal line).
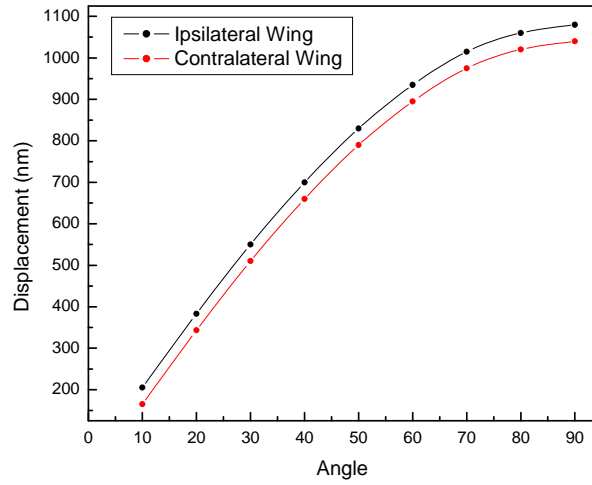
Figure 33.   Amplitudes of Rocking Motion of the two Wings versus Incident Sound
Angle

The vibration amplitudes of both wings of the sensor is an increasing
function of incident angle. An approximate five-fold increase occurs as the
angle increase from 10° to 70°.

In the following section, the experimental data is discussed and compared with
data from the simulations.

D.   AMPLITUDE OF THE DISPLACEMENT OF THE VIBRATION

To collect the data for the rocking frequency of the sensor, a band pass filter is
used to isolate frequencies from 2 to 4 kHz, in order to increase the signal-to-noise ratio.
A sinusoidal sound wave with frequency set at 3 kHz is used in this phase of the
experiment. The sensor has a very stable temporal response, as depicted in Figure 34. The
shape of the sound wave is clearly observed from Figure 34, in which the sensor can
reproduce quite accurately the sinusoidal incident sound wave.
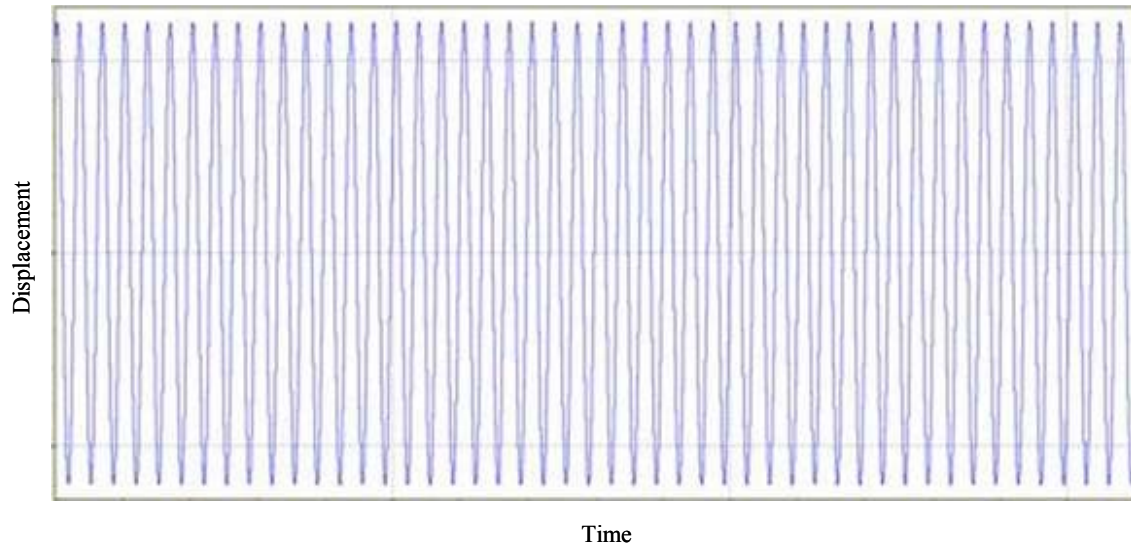
Figure 34.   Displacement of the Sensor as a Function of Time Reproducing the
Sinusoidal Form of the Sound Wave

The amplitude of vibrations of the sensor wings was measured for a set of angles, keeping the sound frequency at 3 kHz and pressure at about 0.1 Pa based on the data from the reference microphone. Figure 35 shows the measured amplitude as a function of the incident angle. It shows an increase of amplitude as the angle is increased, which agrees well with the simulated data in Figure 33. However, it is possible that the variation of sound pressure at different angles arriving at the sensor could also cause it to increase. Such variation can arise from the reflection of sound from the objects surrounding the experimental setup.

49
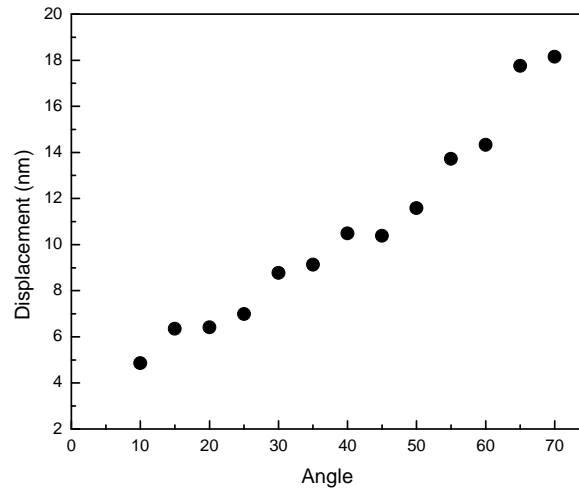
Figure 35.   Measured Amplitude of Vibration of Sensor versus Incident Angle

The first attempt to normalize the data with respect to sound pressure variation was done by dividing each point of the response with its equivalent point of the response of the calibrated reference microphone that was mounted above the sensor as described in Chapter IV. Because the sensor is a narrow-band device, it has a higher signal-to-noise ratio when operated at the resonance frequency of around 3000 Hz. The reference microphone has a broad-band response (20 Hz–20 kHz) and is prone to excess noise even when a band pass filter (2 to 4 kHz) is used. Thus, normalizing the data using the microphone's response could provide misleading information on the directional dependence response of the sensor. Because the simulated displacement of the bending mode remains nearly constant as the incident angle is changed, its amplitude must depend almost exclusively on the pressure of the sound field. This amplitude can be used for normalization of the amplitude at the rocking mode as long as both are measured at the same time. Figure 36 shows the computed values of $\dfrac{A_r}{A_b}$ versus incident angle, where A_r

and A_b are the vibration amplitudes at rocking and bending mode, respectively. At angles other than 45 degrees, the normalized data shows a monotonic increase expected from the

model developed in Chapter I. The anomaly at 45 degrees could be due to undesirable sound reflections from the fixture that holds the sensor chip or the surrounding objects. Further experimentation is needed to understand this behavior.
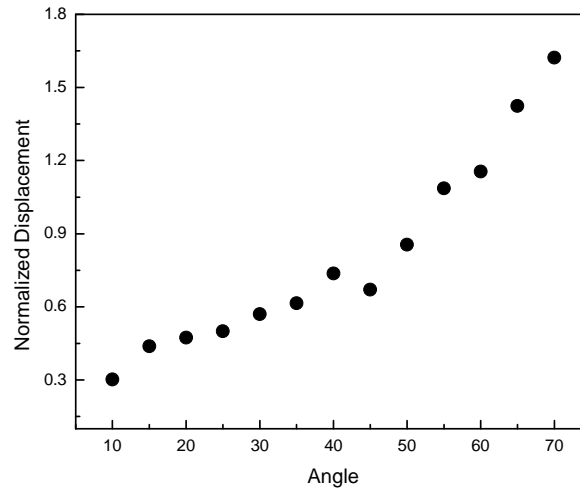
Figure 36.   Normalized Displacement of Sensor versus Incident Angle

Data also were collected to probe the dependence of amplitudes of vibrations of the two wings with the sound pressure. The pressure is measured using the microphone mounted just above the sensor, while the displacement is measured using the laser vibrometer. The results are shown in Figure 37. All measurements were taken at the incident angle of 45 degrees. The wing nearest to the sound source has a greater response than the farther one for the same level of pressure. As the pressure increases, this difference increases, with a value of around 80 nm for a pressure level slightly less than 0.4 Pa.
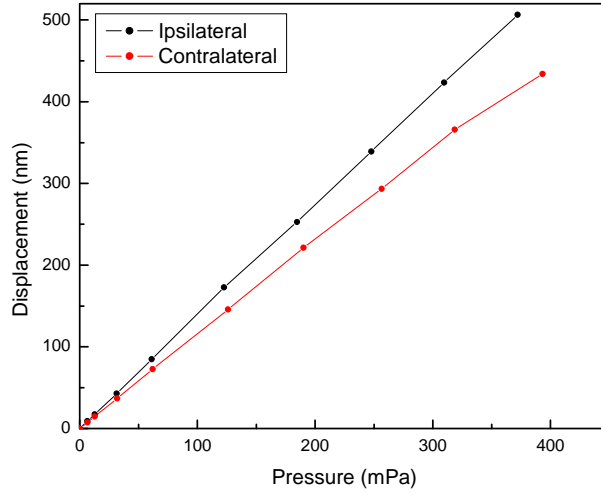
Figure 37.   Measured Amplitudes of the Two Wings versus Pressure of the Sound Wave

E.   DETERMINATION OF THE INCIDENT ANGLE

In order to extract the incident direction of the sound using the amplitudes at the rocking and bending frequencies, a set of data was collected for a sound wave with a known incident angle of 45 degrees. A periodic chirp with a frequency in the 2 to 14 kHz range was used to excite both resonance frequencies of the sensor (rocking and bending) at the same time. A_r and A_b can be expressed in terms of the excitation frequency ω and the sensor parameters as follows:

$$A_r = \frac{Ps}{m}\left[\frac{\sin\left(\frac{\omega\tau}{2}\right)}{\sqrt{\left(\omega_r^2 - \omega^2\right)^2 + \left(\gamma_r\omega\right)^2}}\right]$$

$$A_b = \frac{Ps}{m}\left[\frac{\cos\left(\frac{\omega\tau}{2}\right)}{\sqrt{\left(\omega_b^2 - \omega^2\right)^2 + \left(\gamma_b\omega\right)^2}}\right]$$

(5.3)

52

where m and s are the mass and area of each wing, τ is the time delay between the sound forces on the left and the right wings, and P is the amplitude of the sound pressure, which varies minimally across the sensor's wings due to their relatively small size relative to the length of the sound wave. The specific derivation of these equations was given by Miles, Robert and Hoy [1995] while the modified versions used here are given by Shivok [2007] using the damping coefficients (γ).

These amplitudes, at the respective excitation frequencies, can be obtained from Equation 5.3 as

$$A_r = \frac{P_r}{m}\left[\frac{\sin\left(\frac{\omega_r \tau}{2}\right)}{\gamma_r \omega_r}\right]$$

$$A_b = \frac{P_b}{m}\left[\frac{\cos\left(\frac{\omega_b \tau}{2}\right)}{\gamma_b \omega_b}\right]$$

(5.4)

where P_r and P_b are the pressure of the incident sound wave at the rocking and bending frequency, respectively. Since the time delay τ between the sound forces on the left and the right wings is small, the assumption that $\cos\left(\frac{\omega_b \tau}{2}\right) \approx 1$ is made. Then, the ratio of the two amplitudes can be expressed using Equation 5.4 as

$$\frac{A_r}{A_b} = \frac{P_r}{P_b}\frac{\gamma_b \omega_b \sin\left(\frac{\omega_r \tau}{2}\right)}{\gamma_r \omega_r}.$$

(5.5)

The incident angle ϑ can be obtained by using the relation $\tau = \frac{x * \sin \vartheta}{\upsilon_s}$ as

$$\sin\left(\vartheta\right) = 2\frac{P_b}{P_r}\frac{\gamma_r}{\gamma_b}\frac{1}{\omega_b}\frac{\upsilon_s}{d}\left(\frac{A_r}{A_b}\right).$$

(5.6)

In Equation 5.6, all the parameters can be measured to obtain the incident angle ϑ of the sound wave. The damping coefficients for both resonance frequencies can be

53

estimated by using the full-width half-maximum (FWHM) of the response curve of the sensor at each frequency. Use of the FWHM usually assumes power amplitude; however, in this case the laser vibrometer output was the displacement amplitude. Since the power is proportional to the amplitude squared, full width at square root of two of maximum $\left(FW\sqrt{2}M\right)$ should be used. Figures 38 and 39 show the measured resonance peaks for the bending and rocking modes, respectively. The estimated values of the parameters are given in Table 6.

Parameter	Description	Value
P_r	Sound pressure at rocking frequency	199526.23 µ Pa
P_b	Sound pressure at bending frequency	63095.74 µ Pa
γ_r	Damping coefficient in rocking mode	13 Hz
γ_b	Damping coefficient in bending mode	105 Hz
υ_s	Sound velocity	344 m/sec
d	Distance between the two point forces	1 mm
ω_b	Frequency of bending mode	$2\pi * 10630$ Hz
A_r	Amplitude of vibration in rocking mode	29.23 nm
A_b	Amplitude of vibration in bending mode	31.1 nm

Table 6.   Measured Values for Parameters Estimating Incident Angle
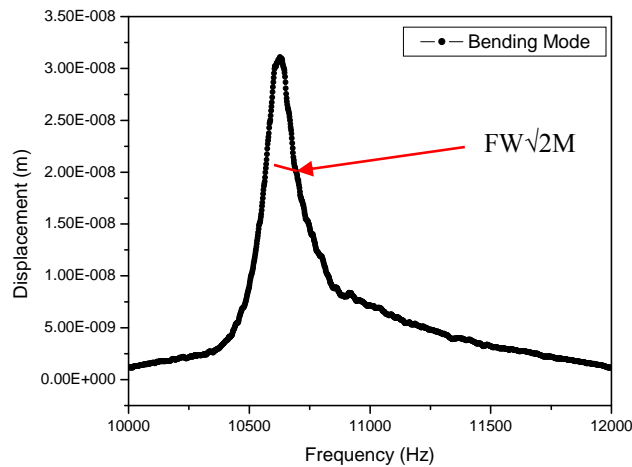
Figure 38.   Measured Resonance Peak for the Bending Mode
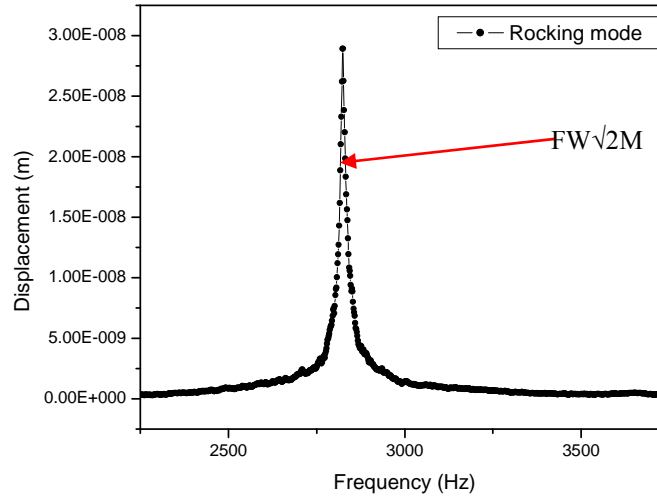
Figure 39.   Measured Resonance Peak for the Rocking Mode

The angle of incident was estimated using the data in Figures 38 and 39 using Equation 5.6 as follows:

$$\sin(\vartheta) = 2 \frac{63095.74}{199526.23} \frac{13}{105} \frac{1}{6.28*10630} \frac{344}{10^{-3}} \left(\frac{29.23}{31.1} \right).$$

$$\sin(\vartheta) = 0.646 \Rightarrow \vartheta \approx 41 \text{ degrees}$$

It can be seen that the angle derived from this approach is in good agreement with the 45 degree incident angle used in the measurement.

F.   DERIVATION OF FREQUENCY RESPONSES IN SPECIFIC CASES

As described in Chapter II, each chip that was used in the experiment has two identical sensors in Positions 8 and 11. Figure 40 presents the response curves for these two sensors on one of the chips.
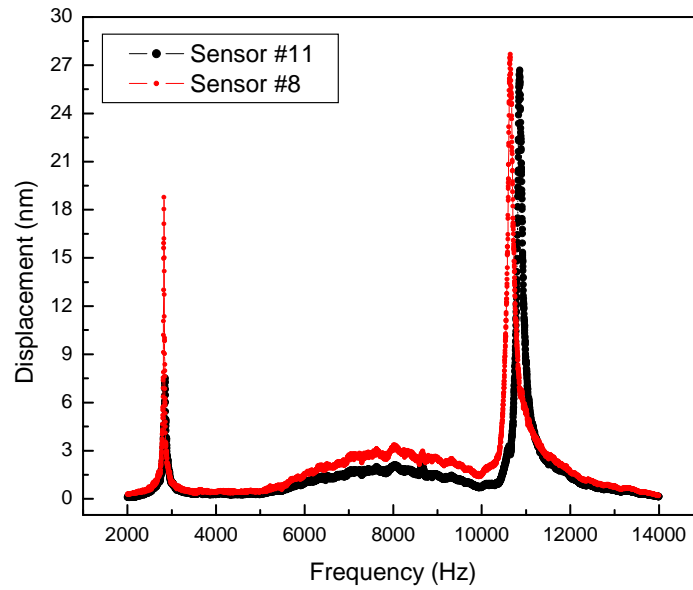
Figure 40.   Frequency Response for Two Identical Sensors

> The figure represents the response curves of two identical sensors for a
> frequency range of 2-14 kHz. Although they are nominally identical, it is
> obvious that one of them has larger amplitude in rocking mode and its
> bending mode peak is shifted to the left.

Both devices exhibit distinct rocking and bending modes during the testing. The
rocking frequency is nearly the same for both sensors, while the bending frequency
appears to have a small difference, on the order of 300 Hz. The displacements of both
devices at the bending mode are almost the same, while a significant difference at the
rocking mode is apparent. The cause of this phenomenon is not clear.

The response curve of Device #10, with perforated wings, is measured and
depicted in Figure 41. Because of the perforated holes at the surface of the sensor, which
cause sound leakage through the holes, the measured displacement is very small (around
0.1 nm) compared with the solid plate sensors that were tested previously.
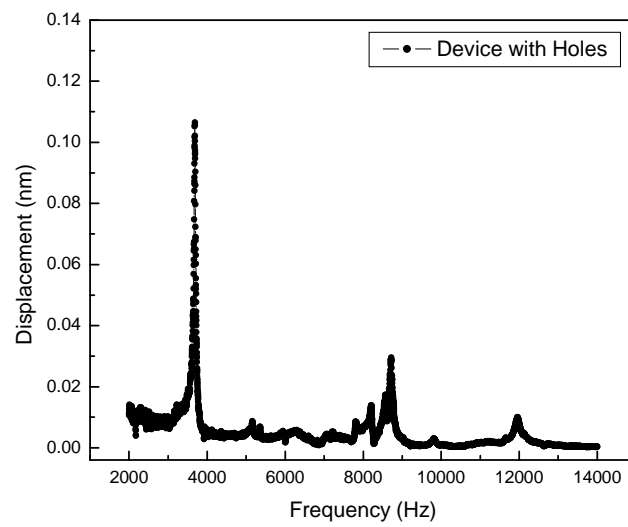
Figure 41.   Frequency Response of Device with Perforated Wings

THIS PAGE INTENTIONALLY LEFT BLANK

VI. ANALYSIS OF EXPERIMENTAL DATA

The objective of the analysis of experimental data described in Chapter IV is to describe, in mathematical terms, the relationship between quantitative characteristics of a sound wave and the performance of the MEMS sound sensor which is studied in this thesis. S-plus® statistical software is used for this analysis. The dependent variable is the vibration amplitude of the sensor's wing, while the quantities used as independent variables in the model are as following:

- Frequency of the sound wave (Hz);
- Intensity of sound (Pa);
- Incident angle of the sound wave.

A. APPROACH

The first priority in building a statistical model is to determine a proper measurement scale for the response variable. It may be worthwhile to consider a transformation of the response variable, in this case the vibration amplitude, if doing so yields a better descriptive model. An analysis of residual and interaction plots guides the search for a transformation, with consideration given to the nature of the response variable. Statistical model-fitting tools for regression and analysis of variance (ANOVA) are then applied to the transformed response variable in order to identify the relationship of the response variable to the independent variables, and to interactions among the independent variables. The analysis is directed to answer the following questions:

- How does the incident angle affect the vibration amplitude of the sensor?
- How does the sound intensity affect the vibration amplitude of the sensor?
- How can differences between the two tested sensors be characterized?
- How can differences between the sensor's two wings be characterized?

B. RESPONSE VARIABLE TRANSFORMATION

The effort of building a model starts by identifying the linear combination of predictor variables that best explains or predicts the vibration amplitude of the sensor.

Using the analysis-of-variance utility in S-Plus, the initial full model includes all potential predictors up to two-way interaction terms as main effect variables. We express the response variable as a linear combination of predictor variables plus an error term. Formally,

$$Y = \beta_0 + \beta_1 X_1 + \beta_2 X_2 + \beta_3 X_3 + \beta_4 X_4 + \beta_{12} X_{12} + \beta_{13} X_{13} + \beta_{14} X_{14} + \beta_{23} X_{23} + \beta_{24} X_{24} + \beta_{34} X_{34} + \varepsilon,$$

(6.1)

where

Y = Vibration amplitude of sensor (nanometers)

X_1 = Incident angle (degrees)

X_2 = Frequency of sound (Hz)

X_3 = Intensity of sound (Pa)

X_4 = Identification of the two identical sensors tested using categorical variable, with values 0 or 1 (0 = sensor # 8, 1 = sensor # 11).

X_{ij} = Interaction between variables X_i and X_j calculated as $X_{ij} = X_i X_j$ ($i, j = 1, \ldots, 4$)

In the above model a full set of predictor variables is included. For this model, there are 120 observations for different level of predictor values as can be seen in Appendix A. Initially, all independent variables are treated as categorical, and all their values are considered distinct factor levels without any numeric properties. The plot of the residuals against the fitted values indicates a non-constant variance of the residuals. Also the normal plot of the residuals shows flattening at the extremes, which is a pattern typical of samples from a distribution with heavier tails than the normal distribution. Therefore a transformation of the response variable with the natural logarithm is used. After transforming the response variable accordingly, the model can be expressed formally as follows:

$$\ln Y = \beta_0 + \beta_1 X_1 + \beta_2 X_2 + \beta_3 X_3 + \beta_4 X_4 + \beta_{12} X_{12} + \beta_{13} X_{13} + \beta_{14} X_{14} + \beta_{23} X_{23} + \beta_{24} X_{24} + \beta_{34} X_{34} + \varepsilon$$

. (6.2)

Transforming the response variable can remove the need for interaction terms, resulting in a more easily interpreted model. Effects that are additive when the response variable is expressed on a logarithmic scale are multiplicative in the original units. For example, the log-additive model given by

$$\ln(Y) = \beta_0 + \beta_1 X_1 + \beta_2 X_2 + \varepsilon,$$

is equivalently expressed as

$$Y = \exp(\beta_0) \times \exp(X_1)^{\beta_1} \times \exp(X_2)^{\beta_2} \times \exp(\varepsilon).$$

If an attempt is made to express the latter in the form of a linear model it will be necessary to introduce product terms that obscure the simplicity of the relationship. Additionally, because the error is expressed as a multiplicative factor, its size in absolute terms will vary with the size of the response function: conditions that lead to small displacements will have small errors and conditions that lead to large displacements will have large errors when measured on an absolute scale. Using a logarithm transformation expresses the error as an additive term with a constant variance.

A comparison of the normal probability plot of the residuals for both cases is depicted in Figure 42.
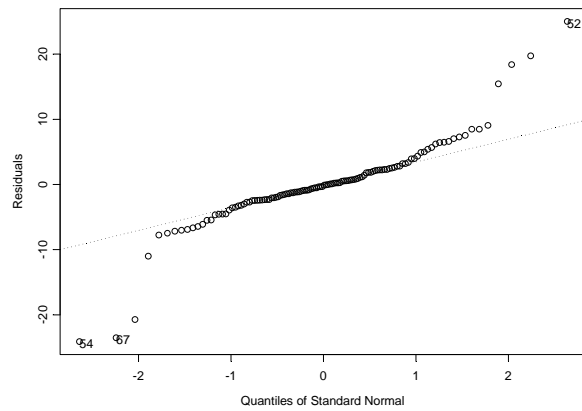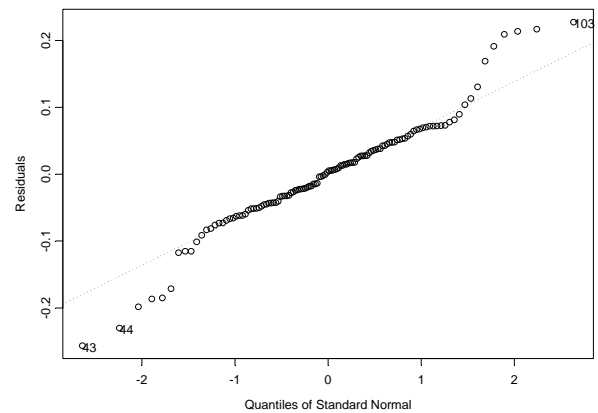
Non- transformed data   Log- transformed data

Figure 42.   Normal Probability Plots of the Residuals

> In the left graph, the normal probability graph of the residuals for a
> response variable in linear scale is depicted, while in the right graph
> a natural logarithmic transformation is used.

It also is useful to examine interaction plots in deciding on the need for a transformation of the response variable. Interaction plots show the values of the response variable in separate trend lines when plotted against the values of two of the independent random variables simultaneously.

Non- transformed data   Log- transformed data
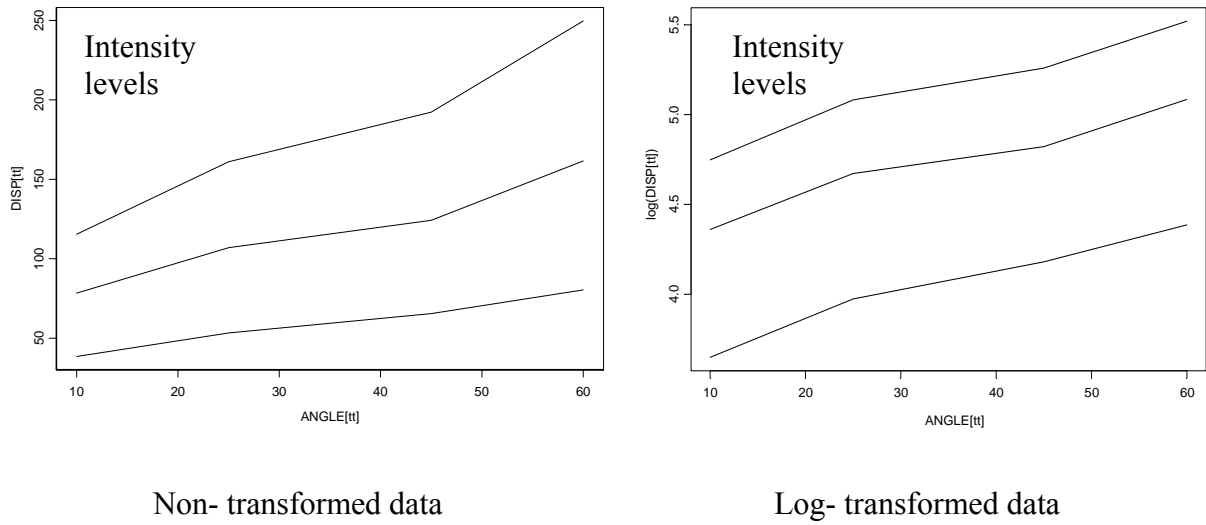
Figure 43.   Interaction Plots of Angle – Intensity versus Displacement

In the left graph, the interaction plot for a response variable in linear scale
can be seen,   while in the right graph a natural logarithmic transformation
is used. DISP [tt] stands for the vibration amplitude of the sensor while
ANGLE [tt] stands for the incident sound angle.

In the first plot (Figure 43a), the trend lines are not parallel, with the gaps
between them increasing as the angle increases.   Normally, this would call for the
inclusion of an interaction terms to account for this effect.   In the second plot (Figure
43b) based on the logarithm of the response variable, the trend lines are nearly parallel to
each other, suggesting that the effects are additive.

A similar pattern is seen in Figure 44, which shows interaction plots for frequency
and intensity of sound.   Again, a logarithm transformation removes the interaction, as
seen in the parallel line plots. This allows the two effects to be expressed additively.

| | Non- transformed data | Log- transformed data |
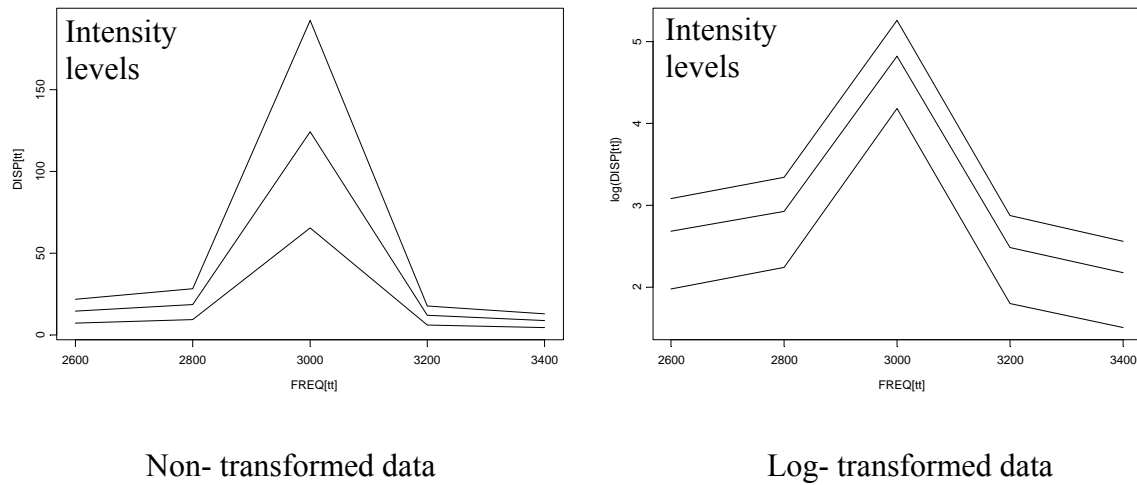
Figure 44.   Interaction Plots of Frequency – Intensity versus Displacement

In the left graph, the interaction plot for a response variable in linear scale can be seen, while in the right graph a natural logarithmic transformation is used. DISP [tt] stands for the vibration amplitude of the sensor while FREQ [tt] stands for the frequency of the sound wave.

C.   INFLUENTIAL FACTORS

The summary output of the analysis of variance of the model described in Equation 5.2 is depicted in Table 7.

	Df	Sum of Sq	Mean Sq	F Value	Pr(F)
ANGLE	3	6.0391	2.01305	180.996	0.0000000
FREQ	4	120.8093	30.20234	2715.531	0.0000000
INTENSITY	2	24.7710	12.38552	1113.598	0.0000000
CONFIG	1	5.1197	5.11970	460.319	0.0000000
ANGLE×FREQ	12	2.2671	0.18892	16.986	0.0000000
ANGLE×INTENSITY	6	0.0022	0.00036	0.032	0.9998469
ANGLE×CONFIG	3	0.9598	0.31992	28.765	0.0000000
FREQ×INTENSITY	8	0.0004	0.00005	0.005	1.0000000
FREQ×CONFIG	4	0.2392	0.05979	5.376	0.0007426
INTENSITY×CONFIG	2	0.0004	0.00021	0.019	0.9809299
Residuals	74	0.8230	0.01112		

Table 7.   Second-Order ANOVA Model Summary

The model includes all two-way interactions. Variables are abbreviated: Freq = frequency, Config = identification of sensor tested. Model terms with P-value less than .05 are statistically significant.

As it is expected from the analysis of previous figures, not all the predictors are significant in the presence of the others, as indicated by their p-values. The interaction terms angle-intensity, frequency-intensity and sensor-intensity appear to be insignificant, in the presence of the other variables in the model.

As can be seen in Table 7, the variable that represents the sensor unit (CONFIG) is highly statistically significant, which suggests that there are differences in the performance of the two sensors that merit examination. The significant interaction terms suggest that on different levels of one variable the effect of the second variable is different. For example the Angle $\times$ Config interaction which is strongly significant suggests that, for different sensor units, the various levels of angle produce different effects. A way to proceed would be to build a different descriptive model for each unit, and identify a region of the design space where the two models coincide, the complementary region being one where differences between units cannot be characterized in simple terms. The latter region would imply idiosyncratic behavior that may point to a need to better control the process for manufacturing the sensors.

In order to evaluate each sensor separately a separate model is fit to each. There are 60 experimental data points for each sensor so the degrees of freedom that can be used to characterize each of them are reduced. For these models, the independent variable Intensity is treated as numeric. Using the notation of Equation 6.2, the model for the first sensor can be expressed:

$$\ln Y = \beta_0 + \beta_1 X_1 + \beta_2 X_2 + \beta_3 X_3 + \beta_{13} X_{13} + \beta_{12} X_{12} + \beta_{23} X_{23} + \varepsilon . \qquad (6.3)$$

The summary output from this analysis of variance model in S-Plus is depicted in Table 8.

```
                       Df Sum of Sq  Mean Sq  F Value      Pr(F)
           ANGLE        3    5.84832  1.94944  210.064 0.0000000
            FREQ        4   62.64892 15.66223 1687.697 0.0000000
       INTENSITY        1   12.20140 12.20140 1314.773 0.0000000
 ANGLE×INTENSITY        3    0.00204  0.00068    0.073 0.9738486
      ANGLE×FREQ       12    2.49238  0.20770   22.381 0.0000000
  INTENSITY×FREQ        4    0.00040  0.00010    0.011 0.9997613
       Residuals       32    0.29697  0.00928
```

Table 8.   Second-Order ANOVA Summary of Sensor 1, S-Plus Report

> The model includes all two-way interactions. Variables are abbreviated in S-Plus: FREQ= frequency. Model terms with P-value less than .05 are statistically significant.

However not all individual variables are significant in the presence of the others, as indicated by their p-values. The intensity-angle as well as frequency-intensity interactions appear to be insignificant, in the presence of the other variables in the model. But differences between sensors reveal a pattern suggesting unit-specific behavior. Figure 45 shows a plot of the differences of the actual amplitudes (after taking logarithms) for the second sensor minus the fitted values obtained from the model based on data from the first sensor.

Both sensors are measured under the same experimental conditions, taken in time sequence. Each sensor proceeds through its 60 measurements in the same order: Intensity cycling through its three levels (.2, .4, .6) within each level of Frequency (2600, 2800, 3000, 3200, 3400) within each level of Angle (60, 45, 25, 10). Positive differences in 58 of the 60 instances suggest that the second sensor gives consistently higher readings than the other. Moreover, the differences increase with the number of runs. This trend may be related to the underlying experimental factors or it may be due to drifting in one of the sensors as the experiment progressed.
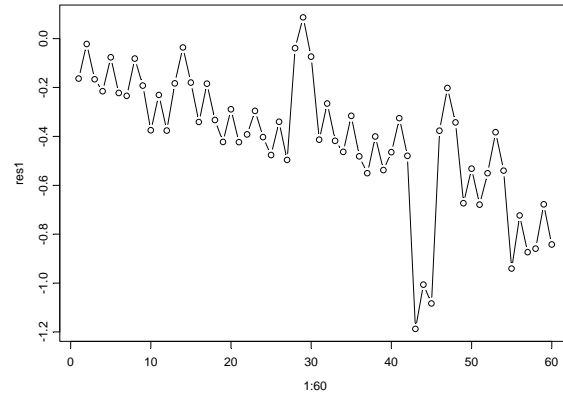
Figure 45.   Comparison of the Two Sensors Data Points

The data points are the differences of actual vibration amplitudes for sensor
2 with the fitted values of model that describe sensor 1. In x-axis the
sequential number of observation can be seen while in y-axis $\ln\left(Y_{0,i}/Y_{1,i}\right)$
is displayed.

Figure 46 shows differences in the measurements between the two sensors on a
logarithmic scale, grouped by Angle. The boxplot show the increasing trend.
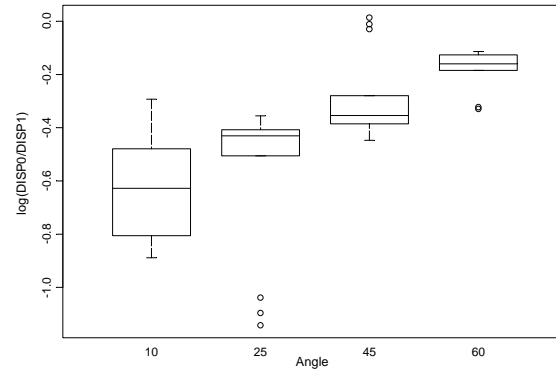
Figure 46.   Differences Between the Two Sensors in Logarithmic Scale for Various
Incident Angles

The box represents all data points of natural logarithm of the difference of
sensors vibration amplitudes for the four levels of angle including all other
potential variability from the other factors. In y-axis $\ln\left(Y_{0,i}/Y_{1,i}\right)$ is
displayed.

67

For this reason, $\ln(Y_{0,i}/Y_{1,i})$ is computed for the data. The previous factor can be re-expressed as $\ln(Y_{0,i}) - \ln(Y_{1,i})$. Assuming $\ln(Y_{0,i}) - \ln(Y_{1,i}) = \beta_0 + \beta_1 X_1 + \varepsilon$, the difference of the two sensors' responses would be proportional to an exponential function of the used parameters $Y_{0,i}/Y_{1,i} = \exp(\beta_0) \times [\exp(X_1)]^{\beta_1} \times \exp(\varepsilon)$. From Figure 46, it can be derived that larger variability between the sensors' responses is occurring for smaller angles. Additionally, it appears that in smaller angles the difference between the two sensors is larger. As the angle increases, the variability of the sensors' responses decrease as does the absolute difference in responses.
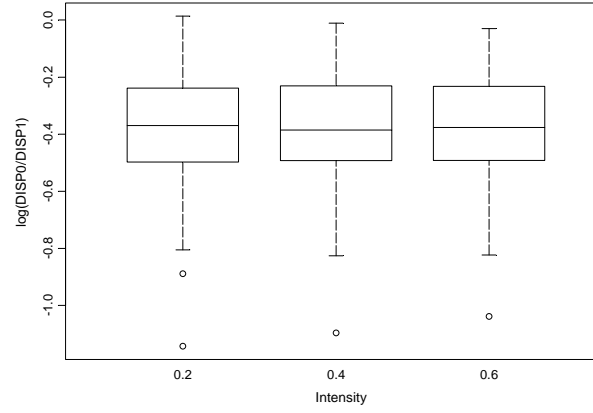
Figure 47.   Comparison of Two Sensors in Logarithmic Scale

   The box represents all data points of natural logarithm of the difference of
   sensors vibration amplitudes for the three levels of intensity including all
   other potential variability from the other factors. In y-axis $\ln(Y_{0,i}/Y_{1,i})$ is
   displayed.

From Figure 47, it is clear that the variability in $\ln(Y_{0,i}/Y_{1,i})$ for the three intensity levels is relatively constant. Also, the mean difference between the two sensors is relatively constant for all the intensity levels. Figure 48 indicates that as the frequency level increases and moves off the resonance frequency, the variability of the sensors' response becomes larger than in the case of the resonant frequency or to a range of 200 Hz around it.
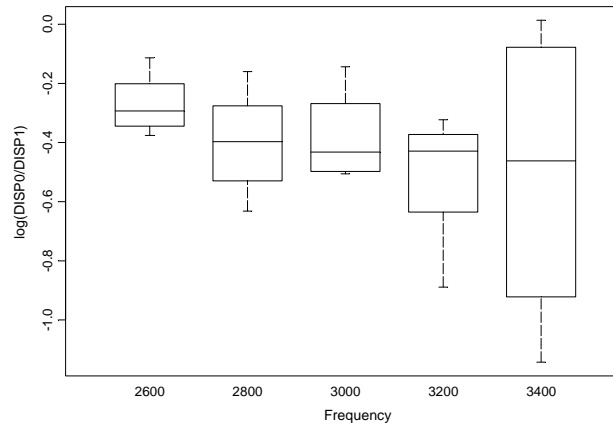
Figure 48.   Differences of the Two Sensors in Logarithmic Scale

The box represents all data points of natural logarithm of the difference of sensors vibration amplitudes for the five levels of frequency including all other potential variability from the other factors. In y-axis $\ln(Y_{0,i}/Y_{1,i})$ is displayed.

|	Df	Sum of Sq	Mean Sq	F Value	Pr(F)
ANGLE	3	1.15058	0.38353	44.088	0.0000000
FREQ	4	58.39959	14.59990	1678.298	0.0000000
INTENSITY	1	12.00645	12.00645	1380.174	0.0000000
ANGLE×INTENSITY	3	0.00006	0.00002	0.002	0.9998574
ANGLE×FREQ	12	0.58587	0.04882	5.612	0.0000452
INTENSITY×FREQ	4	0.00019	0.00005	0.005	0.9999392
Residuals	32	0.27838	0.00870		

Table 9.   Second-Order ANOVA Summary of Sensor 1, S-Plus Report

The model includes all two-way interactions. Variables are abbreviated in S-Plus: FREQ = frequency. Model terms with P-value less than .05 are statistically significant.

From Table 9, the same basic conclusions with the first sensor can be made. The intensity of sound appears to have the same effect in the response variable at any level of frequency. In addition, intensity has the same effect for any level of angle for the specific sensor.

D.   MODEL BUILDING

In order to build a descriptive model with variables treated as numeric, the data points that are around the resonance frequency are used. This means that only frequency levels of 2800 Hz-3000 Hz would be included in the model. This happen in order to better describe the response variable in the region close to resonance frequency of the sensors that is somewhere between 2900-3000 Hz. For the analysis, an ordinary linear regression is used to develop a descriptive model. The final arrangement of the experiment consisted from 4 (Angle) × 3 (Intensity) × 2 (Frequency) × 2 (Sensor), giving a total of 48 experimental runs.

The response variable can be expressed as a linear combination of predictor variables plus an error term as the previous case.

$$\ln Y = \beta_0 + \beta_1 X_1 + \beta_2 X_2 + \beta_3 X_3 + \beta_4 X_4 + \beta_5 X_1^2 + \beta_6 X_3^2 + \beta_{13} X_{13} +$$
$$\beta_{12} X_{12} + \beta_{14} X_{14} + \beta_{23} X_{23} + \beta_{34} X_{34} + \beta_{24} X_{24} + \varepsilon$$

(6.4)

The summary output of this full regression model in S-Plus is given in Table 10.

```
Coefficients:
                  Value  Std. Error  t value   Pr(>|t|)
    (Intercept)   0.7550    0.0834     9.0499    0.0000
          ANGLE   0.0177    0.0024     7.3042    0.0000
           FREQ   1.7262    0.0529    32.6308    0.0000
      INTENSITY   5.5722    0.3541    15.7364    0.0000
         CONFIG   0.6587    0.0529    12.4514    0.0000
        ANGLE^2  -0.0001    0.0000    -3.5230    0.0012
    INTENSITY^2  -3.5489    0.4158    -8.5343    0.0000
ANGLE×INTENSITY   0.0004    0.0025     0.1696    0.8663
     ANGLE×FREQ   0.0039    0.0008     4.7836    0.0000
   ANGLE×CONFIG  -0.0073    0.0008    -8.8788    0.0000
 INTENSITY×FREQ  -0.0006    0.0960    -0.0061    0.9952
INTENSITY×CONFIG -0.0071    0.0960    -0.0738    0.9416
    FREQ×CONFIG  -0.0195    0.0314    -0.6212    0.5385

Residual standard error: 0.05433 on 35 degrees of freedom
Multiple R-Squared: 0.9981
F-statistic: 1543 on 12 and 35 degrees of freedom, the p-value is 0
```

Table 10.   Second-Order model Linear Regression Summary, S-Plus Report

> The model includes all two-way interactions (Equation 6.4). Variables are abbreviated in S-Plus. FREQ = frequency, CONFIG=identification of the sensor tested. Model terms with P-value less than .05 are statistically significant.

The next step is to proceed with stepwise regression to reduce the model to the smallest model that retains significant terms. This is implemented in S-Plus software through the **stepAIC** function implemented in the MASS library [Venables and Ripley, 2002]. Equation 6.5 expresses the reduced model while in Table 11 the summary output can be seen.

$$\ln Y = \beta_0 + \beta_1 X_1 + \beta_2 X_2 + \beta_3 X_3 + \beta_4 X_4 + \beta_5 X_1^2 + \beta_6 X_3^2 + \beta_{12} X_{12} + \beta_{14} X_{14} + \varepsilon \quad (6.5)$$

```
Coefficients:
                Value   Std. Error   t value   Pr(>|t|)
 (Intercept)    0.7555    0.0668     11.3075    0.0000
       ANGLE    0.0179    0.0021      8.5069    0.0000
        FREQ    1.7163    0.0313     54.8749    0.0000
   INTENSITY    5.5833    0.3203     17.4300    0.0000
      CONFIG    0.6461    0.0313     20.6589    0.0000
     ANGLE^2   -0.0001    0.0000     -3.6967    0.0007
 INTENSITY^2   -3.5489    0.3963     -8.9552    0.0000
  ANGLE×FREQ    0.0039    0.0008      5.0195    0.0000
ANGLE×CONFIG   -0.0073    0.0008     -9.3167    0.0000

Residual standard error: 0.05177 on 39 degrees of freedom
Multiple R-Squared: 0.9981
F-statistic: 2548 on 8 and 39 degrees of freedom, the p-value is 0
```

Table 11.   Stepwise Linear Regression Summary, S-Plus Report for Equation 6.5

> Variables are abbreviated in S-Plus. FREQ= frequency, CONFIG=identification of the sensor tested. Model terms with P-value less than .05 are statistically significant.

An initial indication of the model's ability to explain the variance is seen in the Multiple R-squared (R^2) Value. The R^2 value is calculated by dividing the error sums of squares by the total sums of squares and subtracting from 1. Since the response variable is transformed with the natural logarithmic function, this model explains approximately 99.8% of the variability of the natural log of the response variable.

In order to find an equivalent goodness-of-fit measure that applies to the response variable directly, the estimates of $\ln Y_i$ should be converted back to the original units using the exponential function; these are denoted as $\hat{Y}_i$. Because a logarithm

71

transformation is found to be appropriate for linear modeling, it is appropriate to consider a measure that expresses the explanatory power of the model in relative terms. A plausible measure is the average relative error (ARE) defined as follows:

$$\text{ARE} = \frac{1}{n}\sum_{i=1}^{n}\left|\frac{Y_i - \hat{Y}_i}{Y_i}\right|. \tag{6.6}$$

For the model described in Table 11, the ARE is equal to .0038, or 3.80 percent.

E.   MODEL BUILDING FOR RECOLLECTED DATA

Later in the research, another chip nearly identical in design to those already tested was obtained. The chip design is described in Chapter II. The only difference from the previous chips is that a plastic belt was attached around the new chip to improve stability. An absorbing material also was attached close to the back of the sensor in order to mitigate interference with the original sound wave (emanating from the front of the sensor) from a reflected sound wave incident from the back of the sensor. In order to investigate any potential differences in the performance of the sensors of the second chip additional experimental data were collected. The data are reported in Appendix B.

For the analysis of the additional data, an ordinary linear regression is used to develop a descriptive model. All combinations of experimental levels were tested: 3 (Angle) × 3 (Intensity) × 2 (Wing) × 2 (Device) × 2 (Repetition), giving a total of 72 experimental runs.

The 72 observations of this data include four main predictor variables:

X_1 = Incident angle measured in degrees at levels 20, 40 and 60

X_2 = Identification of the sensor's wings using a categorical variable, with values 0 for ipsilateral wing and 1 for contralateral.

X_3 = Intensity of sound measured in Pa at levels 0.2, 0.4 and 0.6.

X_4 = Identification of the two identical sensors tested using categorical variable, with values 0 or 1.

X_{ij} = Interaction between variables X_i and X_j calculated as $X_{ij} = X_i X_j$ $(i, j = 1, \ldots, 4)$

The aims of this analysis are as follows:

- To identify a model that describes both sensors for the resonance frequency of 3000Hz;

- To characterize the effect of the sound on both wings of the sensor (nearest and furthest to the sound source).

The first step is to identify the combination of predictor variables that best explains the vibration amplitude of the sensor. The logarithm of the response variable can be expressed as a linear combination of predictor variables plus an error term as the previous case:

$$\ln Y = \beta_0 + \beta_1 X_1 + \beta_2 X_2 + \beta_3 X_3 + \beta_4 X_4 + \beta_5 X_1^2 + \beta_{13} X_{13} + \beta_{14} X_{14} + \beta_{12} X_{12} + \beta_{23} X_{23} + \beta_{34} X_{34} + \beta_{24} X_{24} + \varepsilon . \quad (6.7)$$

The summary output for the second chip of this full regression model in S-Plus is given in Table 12.

```
Coefficients:
                    Value   Std. Error   t value   Pr(>|t|)
     (Intercept)   2.0707     0.1012     20.4536    0.0000
           ANGLE   0.0741     0.0042     17.7755    0.0000
          ORIENT  -0.2635     0.0675     -3.9044    0.0002
       INTENSITY   2.8269     0.1657     17.0615    0.0000
          CONFIG   0.0958     0.0675      1.4189    0.1611
         ANGLE^2  -0.0005     0.0000    -10.5199    0.0000
 ANGLE×INTENSITY  -0.0010     0.0034     -0.2811    0.7796
    ANGLE×CONFIG  -0.0016     0.0011     -1.4044    0.1654
    ANGLE×ORIENT  -0.0015     0.0011     -1.3837    0.1716
INTENSITY×CONFIG   0.0017     0.1105      0.0153    0.9879
INTENSITY×ORIENT  -0.0247     0.1105     -0.2233    0.8240
   CONFIG×ORIENT   0.0621     0.0361      1.7223    0.0902

Residual standard error: 0.07653 on 60 degrees of freedom
Multiple R-Squared: 0.9905
F-statistic: 571.7 on 11 and 60 degrees of freedom, the p-value is 0
```

Table 12.   Second-Order Model Linear Regression Summary, S-Plus Report for Equation 6.7

The model includes all two-way interactions. Variables are abbreviated in S-Plus. FREQ = frequency, CONFIG = identification of the sensor tested, ORIENT = identification of the sensor's wing that is tested. Model terms with P-value less than .05 are statistically significant.

73

The R^2 value suggests that 99 percent of the variability in the logarithm of displacement is explained by this model. However, not all the variables are significant in the presence of the others, as indicated by their p-values. The sensor-orientation interaction appears to be insignificant, at the five percent level, in the presence of the other variables in this model.

The next step is to proceed with stepwise regression to reduce the model to the smallest model that retains significant terms. This is implemented in S-Plus software as mentioned in the previous section. The stepwise regression analysis identifies that intensity of sound, angle, (angle)^2 and the wing of the sensor as the most significant terms in the model. The sensor variable and also sensor-wing interaction appear to be insignificant at the five percent level but significant at the ten percent level, in the presence of the other variables. Table 13 shows the summary output of the stepwise regression.

```
Coefficients:
                Value Std. Error   t value Pr(>|t|)
  (Intercept)  2.0905    0.0778    26.8640   0.0000
        ANGLE  0.0737    0.0039    19.1367   0.0000
       ORIENT -0.2734    0.0498    -5.4849   0.0000
    INTENSITY  2.7774    0.0540    51.4744   0.0000
       CONFIG  0.0964    0.0498     1.9348   0.0575
       ANGLE^2 -0.0005   0.0000   -10.7681   0.0000
 ANGLE×CONFIG -0.0016    0.0011    -1.4375   0.1555
 ANGLE×ORIENT -0.0015    0.0011    -1.4163   0.1616
 CONFIG×ORIENT 0.0621    0.0352     1.7629   0.0828

Residual standard error: 0.07476 on 63 degrees of freedom
Multiple R-Squared: 0.9905
F-statistic: 823.5 on 8 and 63 degrees of freedom, the p-value is 0
```

Table 13.   Stepwise Regression Summary, S-Plus Report

> Variables are abbreviated in S-Plus. FREQ = frequency, CONFIG = identification of the sensor tested, ORIENT = identification of the sensor's wing that is tested. Model terms with P-value less than .05 are statistically significant.

Since the response variable is transformed with the natural logarithmic function, this model explains approximately 99 percent of the variability of the natural logarithm of the response variable. In order to determine again a measure that expresses the

74

explanatory power of the model in relative terms, ARE as described in previous paragraph is calculated. For the model described in Table 13, ARE is approximately 0.0625, or 6.25 percent. The F-statistic indicates that the model is significant when compared to the intercept-only (β_0-only) model.

From the coefficients of the regression model, the individual variable effects on the natural logarithm of vibration amplitude can be interpreted. Positive coefficients of numerical variables indicate that predicted values of vibration amplitude increase for increasing values of that variable, while for negative coefficients the vibration amplitude decreases for increasing value of that variable. It can be seen that by increasing the incident angle of the sound wave the natural logarithm of vibration amplitude increases with a coefficient equal to 0.0737. The coefficients for categorical variables are interpreted differently. For example, the predicted value of vibration amplitude is computed taking into account the nearest wing of the sensor, so in order to calculate the predicted value of vibration amplitude for the furthest wing, the coefficient of ORIENT equal to $-.2734$ is used. As was expected from the COMSOL simulations and the physics theory, the effects of intensity of sound and the incident angle are positive. The wing of the sensor is depicted as a strongly significant factor on the model which leads to the conclusion that the vibration amplitudes that are produced from the two wings of the sensor are statistically different, with the ipsilateral having larger amplitudes than the contralateral.

A residual analysis on this reduced model is used to check the assumptions of the linear regression model. Plots of the residuals against the fitted values, the responses against the fitted values and the normal quantile plot are studied. As can be seen by these plots, the residuals appear to have fairly constant variance. In addition, they seem to be normally distributed and independent of the fitted values.

In Figure 49, a comparison of the two sensors` responses can be seen. They appear to have nearly the same response function. In each separate graph a comparison between the nearest and the furthest to the sound source wing can be made. The nearest wing appears to have a vibration amplitude at least 100 nm greater than the furthest one,

measured at 60 degrees. Furthermore the difference between the two wings increases for increasing values of angle. All the measurements that are depicted in Figure 49 have been taken for intensity level of 0.6 Pa.

1st Sensor   2nd Sensor
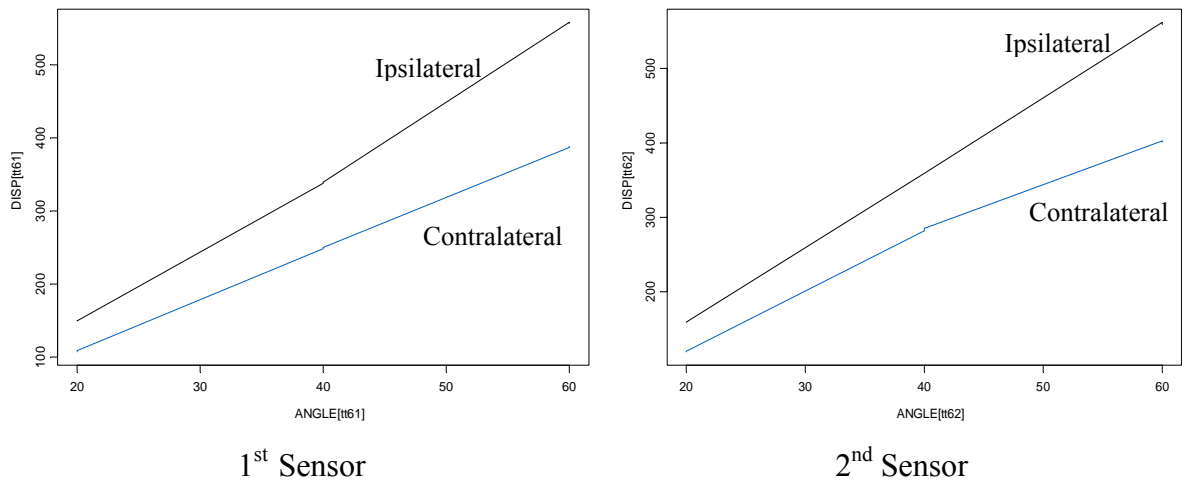
Figure 49.   Interaction Plots of the Vibration Amplitude of the Two Sensors versus Angle

       The plots depict the performance of each sensor in relation to angle. In each plot the response of both wings of the sensor appears (nearest and furthest to sound source). Both plots follow the same scale.

Ipsilateral wing   Contralateral wing
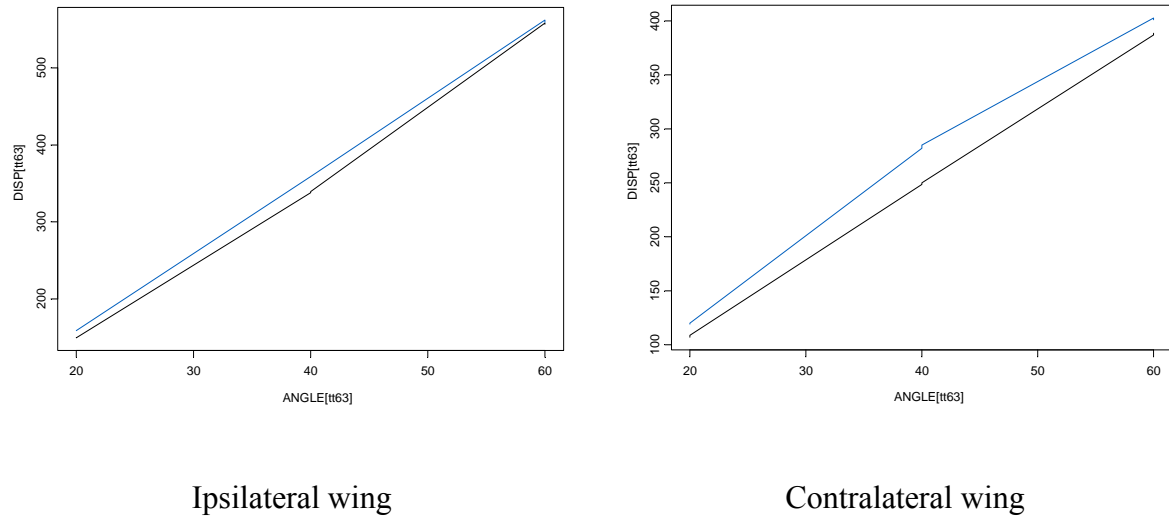
Figure 50.   Vibration Amplitude of the Two Wings versus Angle

The plots depict the performance of each wing as a function of incident
angle. The left graph represents the nearest to the sound source wing while
the right represents the furthest. In each graph the response of both sensors
is depicted in order to compare the similarities of their behavior.

In Figure 50, a comparison of the two wings of each sensor is depicted. As can be
seen to the left graph, the two sensors` performance coincides fairly well in the case of
the nearest wing. On the right graph, there is only a small difference between the furthest
wings of the two sensors. In both cases, the differences between the two prototypes are at
maximum at an angle of 40 degrees. All the measurements of the Figure 50 have been
taken for intensity level of 0.6 Pa.

THIS PAGE INTENTIONALLY LEFT BLANK

VII. CONCLUSIONS AND RECOMMENDATIONS

A. CONCLUSIONS

1. Design of the Sensor

This study has shown that it is possible to fabricate a biomimetic MEMS sensor that displays the expected rocking and bending modes of vibration similar to those of the *Ormia ochracea* fly's hearing system.

The sensors that used for testing were successfully fabricated utilizing the Silicon-on-Insulator Multi-User MEMS process (SOIMUMPs) technology. The measured amplitudes of the sensor's vibrations were found to be of the same order of magnitude as obtained from the simulations. However, the two resonant peaks found to have relatively sharp frequency responses indicating that the damping due to air is not adequate for generating a large amplitude difference between the two sides. Additional damping mechanisms such as squeezed film damping are needed to broaden the peak width to provide enhanced overlapping of the two modes of vibrations. The use of perforated holes on the wings to increase the damping was found to severely reduce the amplitude of vibrations due to leaking of sound pressure through the holes. The answer might be to put holes in a relatively small part of the wings. In this case, the other part of the wings will remain the same and only at the regions of the wings where the holes are located the substrate should not be removed. Simulations showed that such a configuration provides a sensor with a broader frequency response curve. Further research is needed to confirm the simulated performance of the sensor.

2. Significant Variables and Sensor Differences

This study has identified that frequency, intensity of sound and angle of incidence are statistically significant in explaining the variability of the vibration amplitudes. A logarithmic transformation was used to better meet the assumptions of a normal, linear model. It was proven that an increasing incident angle causes the vibration to increase at

79

a rate similar to that of the simulations. The two identically designed sensors seem to behave in a similar way at the range of resonance frequency, but as the frequency of the sound increases, a statistically significant difference between them becomes apparent. The exact cause of this difference is not known at this point but it is possible that the variation of the dimensions during the fabrication can lead to such a behavior.

At the last stage of this research another chip also containing two of those sensors was received. A regression analysis was conducted, in order to further evaluate similarities and differences between the identical units. This study shows almost identical performance from the two sensors in the resonance frequency. In addition, it was verified that the vibration amplitudes of the two wings of each sensor differ significantly which is the key for the fabrication of a perfected sensor.

B.   RECOMMENDATIONS

1.   General

In order to achieve the optimized performance of the sensor, it is recommended that future research could be focused on designing and testing a sensor with solid wings while a portion of it, will be perforated with holes. Damping control can be achieved via selective etching of the substrate under the solid plate while the substrate under the perforated regions. Figure 51 shows a schematic diagram of a possible design of a sensor with partially perforated holes. In this case, simulations should be conducted with slightly different considerations and assumptions. For the solid part of the sensor, the simulation parameters remain the same but for the perforated portions squeezed film damping effects should be incorporated. Squeezed film damping occurs when a thin volume of a gas exists under a moving plate [Bao et al., 2003]. As the plate moves downwards it needs to displace the air underneath. Damping is related to the rate that this displacement occurs. The damping broadens the resonance peak, which is desirable, but it also reduces the vibration amplitude which is undesirable. If the damping is too large the displacement would be nearly eliminated while if the damping is very small the resonance peak would

be very narrow. For this reason, damping is very crucial for this type of sensors and this is the reason why only a small portion of the sensor surface should be perforated to balance the damping and sound coupling.
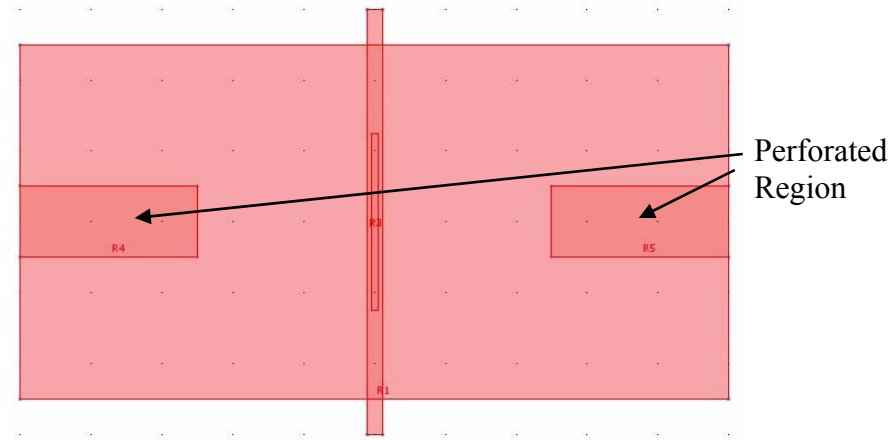
Figure 51.   Possible Sensor Design.

2.   **Experimental Research**

What additional variables, not currently available, would most likely be useful in an explanatory model of vibration amplitude? In this research three variables, (frequency, angle and sound intensity) are studied for their effects on the vibration amplitude. For better evaluation of the sensor's performance several more variables could be studied. As mentioned in Chapter II, every fabricated chip contains around fifteen different sensors. When two identical sensors included in the same chip, are tested, their performance may be affected by each sensor's relative position inside the chip. So, using a variable, which would determine the position of a sensor on the chip, might be helpful in characterizing the sensor. Also, for a sensor with broader resonance modes, more levels of the frequency variable should be used in order to estimate the amplitude vibration in a larger range of frequencies. Additionally, measurements must be taken in different levels of a noisy environment in order to evaluate the effects of noise, if any, on the behavior of the sensor.

C.   FUTURE WORK

There are a number of future research directions for further improving and analyzing the performance of the biomimetic sensor studied in this thesis. Below only a few examples are listed in no particular order of importance.

1.   Areas for Further Work

- Determining bearing resolution of the sensor and also the degradation of the bearing resolution in accordance with the background noise level.

- Packaging issues for the sensor in order to form an integrated autonomic system. Especially if this sensor is going to be used as an underwater device, the differences between the water environment and the air environment need to be considered.

- Estimating the active range of a perfected sensor and verifying operation in a noisy environment (not in a laboratory) taking into account the minimum signal-to-noise ratio of the device.

- Creating an array of perfected sensors and optimizing the parameters of it (shape, number of sensors, etc.).

APPENDIX A. DATA USED FOR THE ANALYSIS OF CHAPTER VI

NUMBER	ANGLE	FREQUENCY	INTENSITY	CONFIGURATION	MEASURED DISPLACEMENT (nm)
1	60	2600	0.2	0	8.6290
2	60	2600	0.4	0	17.2170
3	60	2600	0.6	0	25.8200
4	60	2800	0.2	0	11.8940
5	60	2800	0.4	0	23.7100
6	60	2800	0.6	0	35.5660
7	60	3000	0.2	0	80.3710
8	60	3000	0.4	0	161.5300
9	60	3000	0.6	0	249.6600
10	60	3200	0.2	0	8.0627
11	60	3200	0.4	0	16.1180
12	60	3200	0.6	0	24.1220
13	60	3400	0.2	0	5.7400
14	60	3400	0.4	0	11.4730
15	60	3400	0.6	0	17.1540
16	45	2600	0.2	0	7.2280
17	45	2600	0.4	0	14.6300
18	45	2600	0.6	0	21.8060
19	45	2800	0.2	0	9.4179
20	45	2800	0.4	0	18.6500
21	45	2800	0.6	0	28.2500
22	45	3000	0.2	0	65.4700
23	45	3000	0.4	0	124.2600
24	45	3000	0.6	0	192.3500
25	45	3200	0.2	0	6.0500
26	45	3200	0.4	0	11.9840
27	45	3200	0.6	0	17.7260
28	45	3400	0.2	0	4.5100
29	45	3400	0.4	0	8.8130
30	45	3400	0.6	0	12.9390
31	25	2600	0.2	0	6.6150
32	25	2600	0.4	0	13.3050
33	25	2600	0.6	0	19.8180
34	25	2800	0.2	0	8.5920
35	25	2800	0.4	0	17.3000
36	25	2800	0.6	0	25.4900
37	25	3000	0.2	0	53.2370
38	25	3000	0.4	0	106.9200
39	25	3000	0.6	0	161.0700
40	25	3200	0.2	0	4.7700
41	25	3200	0.4	0	9.5030
42	25	3200	0.6	0	14.1250

NUMBER	ANGLE	FREQUENCY	INTENSITY	CONFIGURATION	MEASURED DISPLACEMENT (nm)
43	25	3400	0.2	0	1.3275
44	25	3400	0.4	0	2.7503
45	25	3400	0.6	0	4.4025
46	10	2600	0.2	0	6.2470
47	10	2600	0.4	0	12.8720
48	10	2600	0.6	0	19.3450
49	10	2800	0.2	0	6.5260
50	10	2800	0.4	0	13.0290
51	10	2800	0.6	0	19.4830
52	10	3000	0.2	0	38.4440
53	10	3000	0.4	0	78.3490
54	10	3000	0.6	0	115.4100
55	10	3200	0.2	0	2.2550
56	10	3200	0.4	0	4.8452
57	10	3200	0.6	0	7.2080
58	10	3400	0.2	0	1.7380
59	10	3400	0.4	0	3.5900
60	10	3400	0.6	0	5.2500
61	60	2600	0.2	1	9.6700
62	60	2600	0.4	1	19.4500
63	60	2600	0.6	1	29.0500
64	60	2800	0.2	1	13.9560
65	60	2800	0.4	1	28.2900
66	60	2800	0.6	1	42.5270
67	60	3000	0.2	1	96.6500
68	60	3000	0.4	1	193.5800
69	60	3000	0.6	1	288.2100
70	60	3200	0.2	1	11.2170
71	60	3200	0.4	1	22.2580
72	60	3200	0.6	1	33.5540
73	60	3400	0.2	1	6.6200
74	60	3400	0.4	1	13.0780
75	60	3400	0.6	1	19.4650
76	45	2600	0.2	1	9.6850
77	45	2600	0.4	1	19.3600
78	45	2600	0.6	1	29.0370
79	45	2800	0.2	1	13.6740
80	45	2800	0.4	1	27.4230
81	45	2800	0.6	1	41.2240
82	45	3000	0.2	1	93.3220
83	45	3000	0.4	1	182.7000
84	45	3000	0.6	1	273.4500
85	45	3200	0.2	1	9.2827
86	45	3200	0.4	1	18.5760
87	45	3200	0.6	1	27.7250

NUMBER	ANGLE	FREQUENCY	INTENSITY	CONFIGURATION	MEASURED DISPLACEMENT (nm)
88	45	3400	0.2	1	4.4500
89	45	3400	0.4	1	8.9100
90	45	3400	0.6	1	13.3300
91	25	2600	0.2	1	9.5500
92	25	2600	0.4	1	18.9800
93	25	2600	0.6	1	28.8530
94	25	2800	0.2	1	13.0850
95	25	2800	0.4	1	26.0100
96	25	2800	0.6	1	39.3190
97	25	3000	0.2	1	87.5760
98	25	3000	0.4	1	177.3100
99	25	3000	0.6	1	261.9400
100	25	3200	0.2	1	7.2220
101	25	3200	0.4	1	14.5430
102	25	3200	0.6	1	21.7250
103	25	3400	0.2	1	4.1627
104	25	3400	0.4	1	8.2300
105	25	3400	0.6	1	12.4350
106	10	2600	0.2	1	8.7213
107	10	2600	0.4	1	17.2940
108	10	2600	0.6	1	25.9330
109	10	2800	0.2	1	12.2800
110	10	2800	0.4	1	24.3580
111	10	2800	0.6	1	36.4930
112	10	3000	0.2	1	63.2200
113	10	3000	0.4	1	126.5400
114	10	3000	0.6	1	189.8300
115	10	3200	0.2	1	5.4834
116	10	3200	0.4	1	11.0670
117	10	3200	0.6	1	16.4160
118	10	3400	0.2	1	3.8890
119	10	3400	0.4	1	7.8375
120	10	3400	0.6	1	11.6100

THIS PAGE INTENTIONALLY LEFT BLANK

APPENDIX B. DATA USED FOR THE ANALYSIS OF SECTION 6E

NUMBER	ANGLE	INTENSITY	CONFIGURATION	ORIENTATION	MEASURED DISPLACEMENT (nm)
1	20	0.2	0	0	48.4
2	20	0.2	0	0	50.3
3	20	0.4	0	0	99.4
4	20	0.4	0	0	98
5	20	0.6	0	0	149.8
6	20	0.6	0	0	149.5
7	40	0.2	0	0	111.5
8	40	0.2	0	0	111.6
9	40	0.4	0	0	224.8
10	40	0.4	0	0	224
11	40	0.6	0	0	338
12	40	0.6	0	0	339.4
13	60	0.2	0	0	183.8
14	60	0.2	0	0	185.8
15	60	0.4	0	0	367.9
16	60	0.4	0	0	369.8
17	60	0.6	0	0	558.2
18	60	0.6	0	0	556.8
19	20	0.2	1	0	49.5
20	20	0.2	1	0	50
21	20	0.4	1	0	100
22	20	0.4	1	0	102
23	20	0.6	1	0	158.8
24	20	0.6	1	0	159
25	40	0.2	1	0	119
26	40	0.2	1	0	117.5
27	40	0.4	1	0	241
28	40	0.4	1	0	239.5
29	40	0.6	1	0	359
30	40	0.6	1	0	359
31	60	0.2	1	0	186.5
32	60	0.2	1	0	187
33	60	0.4	1	0	375
34	60	0.4	1	0	375.8
35	60	0.6	1	0	562
36	60	0.6	1	0	559
37	20	0.2	0	1	35
38	20	0.2	0	1	34.7
39	20	0.4	0	1	70.5
40	20	0.4	0	1	70

NUMBER	ANGLE	INTENSITY	CONFIGURATION	ORIENTATION	MEASURED DISPLACEMENT (nm)
41	20	0.6	0	1	107
42	20	0.6	0	1	108.7
43	40	0.2	0	1	81
44	40	0.2	0	1	82.5
45	40	0.4	0	1	163.5
46	40	0.4	0	1	166.5
47	40	0.6	0	1	248.5
48	40	0.6	0	1	250
49	60	0.2	0	1	129.5
50	60	0.2	0	1	130
51	60	0.4	0	1	259.2
52	60	0.4	0	1	258.8
53	60	0.6	0	1	387
54	60	0.6	0	1	388.5
55	20	0.2	1	1	41.2
56	20	0.2	1	1	40.8
57	20	0.4	1	1	80.3
58	20	0.4	1	1	80
59	20	0.6	1	1	119
60	20	0.6	1	1	120
61	40	0.2	1	1	93
62	40	0.2	1	1	92.8
63	40	0.4	1	1	188.3
64	40	0.4	1	1	188.5
65	40	0.6	1	1	282
66	40	0.6	1	1	285
67	60	0.2	1	1	132
68	60	0.2	1	1	132.5
69	60	0.4	1	1	266.5
70	60	0.4	1	1	266
71	60	0.6	1	1	402.7
72	60	0.6	1	1	401

LIST OF REFERENCES

Bao, M., Yang, H., Sun, Y., Wang, Y. (2003, November). Squeeze-film air damping of thick hole-plate. *Sensors and Actuators A: Physical,* 108, 212–217.

Box, G.E.P., Hunter, W.G., and Hunter, J.S. (2005). *Statistics for Experimenters,* 2nd ed., John Wiley & Sons, New Jersey.

Cade, W., (1975, December). Acoustically orienting parasitoids: fly phonotaxis to cricket song. *Science*, 190, 1312–1313.

Federation of American Scientists (FAS). Retrieved January 2008 from, http://www.fas.org/man/dod 101/navy/docs/es310/asw_sys/asw_sys.htm.

Holmes, J.D., Carey, W.M., Lynch, J.F., Newhall, A.E., and Kukulya, (2005, June). A. An Autonomous Underwater Vehicle Towed Array for Ocean Acoustic Measurements and Inversions, *Oceans 2005-Europe*, 2, 1058–1061.

Leiritronica Portugal - Selenium Loudspeakers. Retrieved May 2008 from, http://www.audio.leiritronica.pt/images/pdf/DH200E.pdf.

Liu, C. (2006). *Foundations of MEMS,* New Jersey: Pearson education.

Master Catalog, Electronic Instruments. (1989). Bruel & Kjaer Instruments, Inc., 175–190.

Michelsen, A. (1992). Hearing and sound communication in small animals: evolutionary adaptations to the laws of physics. In D.B. Webster, R.R. Fay, A.N. Popper (Ed.), *The Evolutionary Biology of Hearing* (pp. 61–77). New York: Springer-Verlag.

Miles, R.N., Robert, D., and Hoy, R.R. (1995, December). Mechanically coupled ears for directional hearing in the parasitoid fly *Ormia ochracea*. *The Journal of the Acoustical Society of America*, 98, 3059–3070.

Miller, K., Cowen, A., Hames, G., and Harby, B. (2004). *SOIMUMPS, Design Handbook,* 4th ed.

Newell, W. E. (1968, September). Miniaturization of Tuning Forks. *Science*, *27*(161), 1320–1326.

Polytec User Manual. (2007). Fiber–coupled Vibrometer Sensor Head OFV – 53.

Rao, S.S. (2003). *Mechanical Vibrations*, 4th ed. New Jersey: Pearson Education, Inc.

Robert, D., Read, M. P., and Hoy, R.R. (1996, January). The tympanal hearing organ of the parasitoid fly *Ormia ochracea* (Diptera, Tachinidae, Ormiini). *Cell and Tissue Research*, 275, 63–78.

Shivok, T.J. (2007, September). *Mems Polymumps-Based Miniature Microphone for Directional Sound Sensing*, Master's Thesis, Monterey, CA: Naval Postgraduate School.

Venables, W.N., and Ripley B.D. (2002). *Modern Applied Statistics with S,* 4th ed. New York: Springer.

Zhang, W., and Turner, K. (2006, July). Frequency dependent fluid damping of micro/nano flexural resonators: Experiment, model and analysis. *Sensors and Actuators A: Physical,* 134, 594–599.

INITIAL DISTRIBUTION LIST

1. Defense Technical Information Center
    Ft. Belvoir, Virginia

2. Dudley Knox Library
    Naval Postgraduate School
    Monterey, California

3. James Luscombe, Chairman Physics
    Naval Postgraduate School
    Monterey, California

4. James Eagle, Chairman Operations Research
    Naval Postgraduate School
    Monterey, California

5. Associate Professor Gamani Karunasiri
    Naval Postgraduate School
    Monterey, California

6. Associate Professor Robert Koyak
    Naval Postgraduate School
    Monterey, California

7. Antonios Dritsas
    Naval Postgraduate School
    Monterey, California